




Charged Particle Oscillations around a black hole Surrounded by CDM Halos

Z. Ahal ^{1*}, H. El Moumni ^{1†}, K. Masmar ^{1‡}

¹ LPTHE, Physics Department, Faculty of Sciences, Ibnou Zohr University, Agadir, Morocco.

July 16, 2025

Abstract

HF QPOs are among the most intriguing phenomena observed in LMXBs containing BHs or neutron stars. In this work, we investigate charged particles' dynamics in the nearby of a Schwarzschild-like BH embedded in a uniform magnetic field and surrounded on all sides by CDM. Thereby gaining deeper insight into the influence of magnetic and DM distributions on observable phenomena near compact objects. We first present a modified metric, which incorporates the effects of a CDM, and we explore how both DM and magnetic fields influence the effective potential, stable circular orbits, and escape conditions for ionized particles. Employing a Hamiltonian formalism, we analyze the energy boundaries and ISCO, demonstrating that CDM causes an outward shift of the ISCO, while magnetic fields tend to pull it closer to the event horizon.

We compute the fundamental oscillation frequencies—radial, latitudinal, Keplerian, and Larmor—and demonstrate how their variation depends on the combined influence of CDM and magnetic field strength. The resulting frequency structure allows us to identify resonance radii associated with HF QPOs, particularly those in 3:2 ratios observed in microquasars. We assess several theoretical models for QPO generation, including the (ER), Relativistic Precession (RP), Tidal Disruption (TD), and Warped Disk (WD) models. A comparative fit of observational data from GRS 1915+105, H1743-322, XTE 1550-564, and GRO 1655-40 demonstrate that the TD and WD models provide the best match for HF QPOs in the presence of moderate magnetic flux ($B' = 0.1$), while the other models except ER fit better in weak-field scenarios.

Our results highlight the importance of including both magnetic and dark matter (DM) effects in strong-field astrophysics and support the use of HF QPOs as sensitive probes of BH environments. This study opens new perspectives for exploring particle dynamics, accretion disk structure, and observational signatures of DM near compact objects.

Contents

1	Introduction	2
2	Schwarzschild BH solution surrounded by the CDM: some geometrical implications	4

*zakaria.ahal@edu.uiz.ac.ma

†h.elmoumni@uiz.ac.ma

‡k.masmar@uiz.ac.ma (Corresponding author)

3	Particle dynamics in magnetized BH surrounded by CDM halos	7
3.1	Magnetized BH solution with CDM	7
3.2	Charged particle dynamics: Hamiltonian and effective potential	8
3.3	More on curled trajectories	16
4	Harmonic oscillations of a charged particle in a magnetized BH with CDM halos	17
4.1	Ionized particles and jet particles	19
4.2	Resonance Radii	21
5	On some astrophysical estimations of HF QPOs	25
6	Conclusion and Discussion	28

1 Introduction

High-frequency quasi-periodic oscillations (HF QPOs) observed in the X-ray flux of low-mass X-ray binaries (LMXBs) consisting of BHs (BHs) or neutron stars offer a valuable insight into the physics of strong gravitational fields [1–3]. These oscillations, typically appear as twin peaks in the power spectral density of X-ray observations, exhibit characteristic frequencies in hundreds of hertz. Remarkably, in many cases, the captured frequencies of HF QPOs appear in a commensurate 3:2 ratio, suggesting the presence of resonant processes in the inner accretion disk region [4, 5].

The study of HF QPOs is of significant astrophysical importance, as their frequencies are believed to be directly linked to the fundamental properties of the compact object, including its mass, spin, and the spacetime geometry near the event horizon [6]. Various theoretical frameworks have been suggested to explain the origin of HF QPOs, ranging from relativistic precession and disk oscillation models to non-linear resonances between different oscillation modes in the accretion flow [7, 8]. More recently, the role of electromagnetic interactions, particularly in systems with strong magnetic fields, has been explored as a potential contributor to HF QPOs formation [9, 10].

In addition to classical general relativity frameworks, modifications to black hole (BH) spacetimes arising from quantum gravity corrections and alternative theories of gravity have been investigated through HF QPOs [11, 12]. Quantum-corrected BHs, regular BHs with modified cores, and deviations from Kerr or Schwarzschild solutions can introduce perturbations in the epicyclic frequencies of accreting particles, thereby influencing the HF QPOs spectrum [13, 14]. Observational constraints on these models indirectly test fundamental physics beyond Einstein’s theory of general relativity.

The Cold DM (CDM) paradigm, which posits that DM is composed of non-relativistic, collisionless particles, has proven remarkably effective at explaining large-scale cosmological phenomena. It unveils an excellent fit to the observed temperature anisotropies in the Cosmic Microwave Background (CMB), the matter power spectrum, and the distribution and abundance of galaxy clusters [15, 16]. According to this model, DM must be electrically neutral or, if charged, have a charge significantly less than that of the electron—unless in the exceptionally massive particles [17–20]. This leaves open the possibility of DM being made of millicharged particles characterized by a fractional electric charge, where such particles naturally arise in various extensions of the Standard Model [21, 22]. These hypothetical particles may be either fermionic or bosonic.

Although the CDM model reliably predicts the hierarchical expansion of the cosmic structure on large scales, it faces challenges at galactic and subgalactic scales. Discrepancies have emerged from comparisons between simulations and observational data, particularly in the context of the Local Group’s dwarf satellite galaxies [16]. These satellites, being dark-matter-dominated systems, serve as critical laboratories for testing the microphysics of DM. The advent of ultra-faint dwarf galaxy discoveries has addressed some earlier concerns, such as the “missing satellites” problem [23], but newer issues have arisen. Notably, simulations predict an overabundance of dense subhaloes that are too massive to correspond to the brightest observed of the Milky Way satellites, a problem known as “too big to fail” [24]. Additionally, the observation that satellite galaxies around both the Milky Way and Andromeda tend to lie in vast, rotating planar structures remains an unexplained anomaly within the standard CDM framework [25, 26].

The Event Horizon Telescope (EHT) has marked a milestone in BH research by capturing the first images of BHs. The 2019 image of M87* and the 2022 image of Sgr A* revealed bright, ring-like structures surrounding dark centers, offering the most direct visual evidence of BH existence to date [27, 28]. BHs are not anticipated to exist in complete isolation. In realistic astrophysical settings, they are typically embedded in dynamic and complex environments. In particular, there is compelling evidence that supermassive BHs play a fundamental role in powering active galactic nuclei [29, 30], where the complex surroundings consist of ionized plasma, electromagnetic fields, and DM [31]. Consequently, the presence of a dark-matter halo near these compact objects is anticipated to influence the motion of surrounding matter and may leave observable signatures in the form of altered gravitational wave emissions from such galactic environments [32].

Particle dynamics near BHs is of considerable interest due to the valuable insights they provide into the geometry and nature of the surrounding spacetime. A particularly notable feature is the existence of a limiting radius, known as the innermost stable circular orbit (ISCO), beyond of which stable circular motion cannot exist. When a particle reaches this boundary, it cannot maintain a stable orbit and is eventually drawn into the BH [33–35]. In this sense, a substantial body of work has examined the charged particles behavior near BHs situated within external magnetic force [36–39]. Observations suggest that strong magnetic fields exist near BHs, varying in mass. For instance, fields can reach magnitudes of 10^8 G around stellar-mass BHs and about 10^4 G for supermassive ones, whereas Sgr A* is estimated to have a weaker field of approximately 10–100 G [36, 40]. The influence of magnetic fields on particle motion near BHs is often modeled using the Wald solution, which reveals chaotic trajectories for charged particles due to deviations from the equatorial plane [41].

Beyond the Schwarzschild BH model, which reveals an ISCO at $6M$ [36], more complex models involving Kerr BHs surrounded by various magnetic field configurations have also been explored [42–44]. These studies highlight the need to account for surrounding matter fields, as BHs are nonexistent in a vacuum. One such key component of the astrophysical environment is DM (DM), whose existence was first inferred from the rotational curves of spiral galaxies, where BHs are commonly found at their centers [45].

The combination of gravitational, electromagnetic, and DM effects offers a more realistic setting to analyze BH environments [45–47]. Furthermore, both magnetic fields and DM significantly influence the dynamics of the accretion disk. Strong magnetic fields are known to be responsible for relativistic jets, while DM affects the disk’s luminosity [48]. Among the observable features of accretion disks are high-frequency quasiperiodic oscillations (HF QPOs), which reflect the properties of the gravitational field near BHs. HF QPOs have been detected in microquasars such as GRS 1915+105, H1743-322, XTE 1550-564 and GRO 1655-40 [36, 49], and their origin is closely related to the particles trajectories around compact objects and continues to be a topic of extensive study [47, 50, 51].

It is particularly compelling to investigate the interplay between gravity, magnetic fields (MF), and DM (DM) in the surrounded of BHs, as these components significantly alter the spacetime geometry. Various models of DM halos have been suggested, including perfect fluid DM (PFDM), scalar field DM (SFDM), warm DM (WDM), and cold DM (CDM) [52, 53]. In this work, we focus on the Schwarzschild BH Exposed to a uniform magnetic field and surrounded by a CDM halo, as a representative scenario for exploring the charged particles dynamics under the coupled influence of gravitational, electromagnetic, and DM fields.

This study primarily seeks to contribute to this interesting area of gravitational physics. Indeed, we attempt to understand how charged-particle behavior is affected by the simultaneous presence of strong magnetic fields and high DM density. We first present a modified Schwarzschild metric that incorporates the effects of a CDM halo. Then, using the Hamiltonian formalism, we obtain the effective potential governing the trajectory of a charged particle, allowing us to analyze its energy, angular momentum, and orbital stability.

Furthermore, we extend our investigation to examine the quasi-periodic oscillations (QPOs) of charged particles in this environment. Specifically, we aim to characterize the epicyclic frequencies of particles orbiting a Schwarzschild BH embedded in a uniform magnetic field and surrounded by CDM, thereby gaining deeper insight into the influence of these fields on observable phenomena near compact objects.

This paper is structured as follows. In Sec. 2, we revisit the Schwarzschild metric modified by the presence of CDM and discuss its key geometrical implications. Sec. 3 is committed to the study of charged particle dynamics in the vicinity of the modified Schwarzschild BH, embedded in a uniform magnetic field and surrounded by CDM. We analyze the effective potential, angular momentum, energy, and the ISCO under various conditions, including the presence or absence of CDM, and explore the effects of varying CDM density. In Sec. 4, we examine the harmonic oscillations of charged particles around the magnetized BH in a CDM environment. Special emphasis is put on the behavior of ionized particles, jet-like trajectories, and the resonant radii associated with twin-peak HF QPOs, particularly focusing on the 3:2 ratio between upper and lower frequencies. Sec. 5 presents astrophysical estimations of the HF QPOs, and we perform a comparative analysis by fitting observed HF QPOs data from microquasars within different theoretical models. Finally, the last section concludes the paper with a summary of the main results along with a discussion of their broader implications.

2 Schwarzschild BH solution surrounded by the CDM: some geometrical implications

In the following section, we unveil a specific form of the Schwarzschild spacetime modified by the presence of CDM. The CDM distribution is modeled using the Navarro–Frenk–White (NFW) density profile, which arises from large-scale numerical simulations within the CDM framework [54, 55]. The resulting spacetime describes a static, spherically symmetric, uncharged, and non-rotating BH embedded in a CDM halo, and is expressed by the following metric [56]:

$$ds^2 = -f(r) dt^2 + g^{-1}(r) dr^2 + r^2 d\theta^2 + r^2 \sin^2 \theta d\phi^2 \quad (1)$$

The CDM density profile is commonly modeled by the NFW profile, which is derived from cosmological N-body simulations [56]. The radial density distribution is indicated by

$$\rho_{NFW}(r) = \frac{\rho_s}{\frac{r}{R_s} \left(1 + \frac{r}{R_s}\right)^2}, \quad (2)$$

where ρ_s is the characteristic (core) density and R_s is the scale (characteristic) radius of the halo. The mass enclosed within a radius r , corresponding to a general spherically symmetric density distribution $\rho(r)$, is defined by

$$M_{DM}(r) = 4\pi \int_0^r \rho(r') r'^2 dr' \quad (3)$$

Applying this to the NFW profile, the mass confined within radius r becomes

$$M_{NFW}(r) = 4\pi \int_0^r \rho_{NFW}(r) r^2 dr. \quad (4)$$

which yields the analytical expression

$$M_{NFW}(r) = 4\pi\rho_s R_s^3 \left(\ln \left(1 + \frac{r}{R_s} \right) - \frac{\frac{r}{R_s}}{\left(1 + \frac{r}{R_s} \right)} \right). \quad (5)$$

Using Kepler's third law, the rotational velocity of a particle under the influence of this mass distribution is obtained to be

$$V(r) = \sqrt{\frac{GM(r)}{r}}. \quad (6)$$

Substituting the NFW mass profile into this relation, the rotational velocity becomes

$$V_{NFW}(r) = \sqrt{(4\pi\rho_s G R_s^3) \frac{1}{r} \left[\ln \left(1 + \frac{r}{R_s} \right) - \frac{\frac{r}{R_s}}{\left(1 + \frac{r}{R_s} \right)} \right]}. \quad (7)$$

To relate this to spacetime geometry, we consider the modified Schwarzschild metric with a CDM halo, in which the metric coefficient is denoted by $f(r) = g(r)$. The rotational particle velocity in the equatorial plane ($\theta = \pi/2$) is derived from the metric as

$$V^2 = r \frac{d \ln(\sqrt{f(r)})}{dr} \quad (8)$$

Solving for the metric function $f(r)$, one obtains

$$f(r) = \left[1 + \frac{r}{R_s} \right]^{-\frac{8\pi G \rho_s R_s^3}{r}}. \quad (9)$$

Given that BHs are usually located at galactic centers, it is natural to expect them to be embedded within DM halos. To investigate the influence of DM on the structure of the surrounding spacetime, we begin by introducing an effective energy-momentum tensor that accounts for the influence of the DM halo, denoted as

$$T_\mu^\nu = \begin{pmatrix} -\rho & 0 & 0 & 0 \\ 0 & p_r & 0 & 0 \\ 0 & 0 & p_\theta & 0 \\ 0 & 0 & 0 & p_\phi \end{pmatrix}. \quad (10)$$

Under the framework of General Relativity, the Einstein field equations connect spacetime geometry to the distribution of energy and momentum through the energy-momentum tensor.

$$G_\mu^\nu = kT_\mu^\nu, \quad (11)$$

where $k = 8\pi G/c^4$ is the Einstein gravitational constant. The Einstein tensor G_μ^ν is defined as

$$G_\mu^\nu = R_\mu^\nu - \frac{1}{2}g_\mu^\nu R, \quad (12)$$

with R_μ^ν being the Ricci tensor, R the Ricci scalar, and g_μ^ν the metric tensor. The Einstein field equations can be modified to incorporate the influence of a DM halo surrounding the BH by introducing an effective energy-momentum tensor, leading to the form

$$G_\mu^\nu = k(T_\mu^\nu + T_\mu^{\nu(DM)}). \quad (13)$$

We are now in a position to propose an extended form of the Schwarzschild metric that incorporates the gravitational influence of a surrounding CDM halo, given by:

$$ds = -(f^*(r) + f(r))dt^2 + (f^*(r) + f(r))^{-1}dr^2 + r^2 dr^2 + r^2 \sin^2 \theta \quad (14)$$

Including both energy-momentum tensors ensures that the solution simplifies to the standard Schwarzschild metric without a DM halo. Further details of this approach can be found in [56]. The resulting modified Schwarzschild metric, accounting for the gravitational effects of a CDM halo, takes the form of the blackening function:

$$f^*(r) + f(r) = \left(1 + \frac{r}{R_s}\right)^{-\frac{8\pi G \rho_s R_s^3}{c^2 r}} - \frac{2GM}{rc^2}. \quad (15)$$

Let us denote $\kappa = \rho_s R_s^3$, a parameter that characterizes the CDM profile alongside R_s . These parameters contribute substantially in controlling the behavior and physical influence of the distribution of DM. To provide insights into the dark-matter geometrical consequence, the embedding diagram of such a BH within several values of κ quantity is depicted in Fig. 1. For the remainder of the paper, we fix the characteristic radius value R_s , such that the influence of DM is fully captured through variations in the parameter κ .

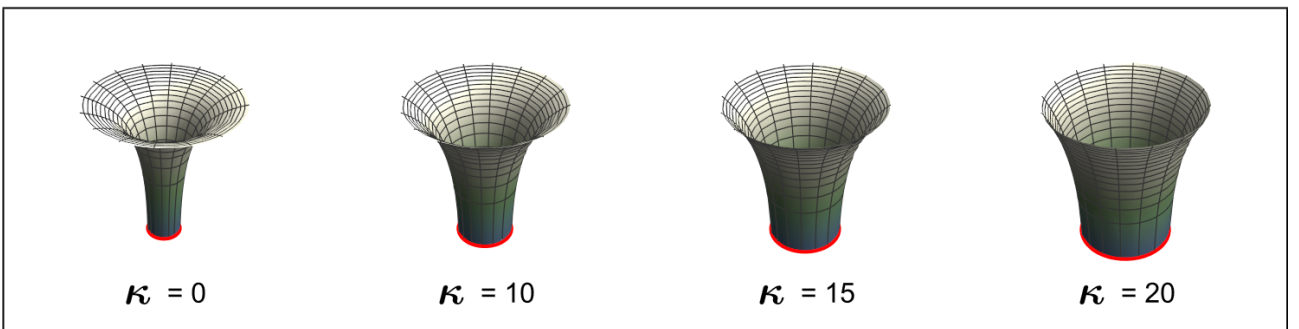


Figure 1: Embedding diagram within different values dark-matter parameter κ . The red circle represents the BH event horizon.

Initially, we examine the limiting case where DM is absent to explore the physical implications of the modified metric incorporating DM. In this scenario, the metric diminishes to the standard Schwarzschild solution, which the singularity located at $r = 0$ and possesses an event horizon located at $r_h = 2M$. When DM is present, the spacetime geometry is influenced by the parameter κ , which governs the modifications introduced by the surrounding halo. In particular, as the parameter κ increases, both the size of the BH core and the radius of the

event horizon grow. The location of the event horizon is determined by solving the following equation:

$$\left(1 + \frac{r}{R_s}\right)^{-\frac{8\pi G\kappa}{c^2 r}} - \frac{2GM}{rc^2} = 0. \quad (16)$$

Having revisited the BH solution embedded in a CDM and unveiled the effect of the κ parameter on the spacetime geometry, our attention is drawn to disclose the charged particle dynamics in such a magnetized BH background.

3 Particle dynamics in magnetized BH surrounded by CDM halos

3.1 Magnetized BH solution with CDM

This study focuses on the orbital dynamics of particles with $q \neq 0$ and mass m in the vicinity of a BH embedded within a uniform magnetic field, taking into account the presence of a surrounding CDM halo. The underlying spacetime is represented by the blackening function in Eq.(15).

Such a stationary and axial symmetry unveils timelike and spacelike killing vectors obtained by the equation [36, 41]

$$\partial\xi_{\alpha,\beta} + \partial\xi_{\beta,\alpha} = 0. \quad (17)$$

The expression for the four-vector potential A^μ , which describes the test electromagnetic field, is expressed as [36, 41]

$$A^\mu = C_1\xi_{(t)}^\mu + C_2\xi_{(\phi)}^\mu, \quad (18)$$

with $C_{1,2}$ are integration constants. Giving that the BH is situated in a uniform magnetic field B , the associated electromagnetic field tensor F must satisfy the conditions established by Wald [41]. Specifically, F must be stationary and axially symmetric, regular (i.e., non-singular) across the event horizon, and asymptotically approach a uniform magnetic field of strength B at spatial infinity [41]. Under these conditions, the electromagnetic field tensor be formulated as

$$F = \frac{1}{2}B \left(d\xi_{(\phi)} + \frac{2J}{M}d\xi_{(t)} \right), \quad (19)$$

in which J and M represent the mass and angular momentum of the BH, respectively.

Accordingly, the four-vector potential is given by [41]

$$A^\mu = \frac{1}{2}B \left(\xi_{(\phi)}^\mu + \frac{2J}{m}\xi_{(t)}^\mu \right) \quad (20)$$

With regard to of a non-rotating (Schwarzschild) BH, where $J = 0$, the four-vector potential simplifies to

$$A^\mu = \frac{1}{2}B, \xi_{(\phi)}^\mu, \quad (21)$$

With $\xi_{(\phi)}^\mu = \partial/\partial\phi$. The covariant component A_ϕ of the potential, then takes the form

$$A_\phi = \frac{1}{2}Bg_{\phi\phi}, \quad (22)$$

where $g_{\phi\phi}$ is the corresponding component of the spacetime metric Eq.(1). The motion of a particle with mass m and charge q in this background is governed by the Lorentz force equation

$$m\dot{u}^\mu = qF^\mu_\nu u^\nu. \quad (23)$$

\dot{u}^μ refers to the particle four-velocity with the normalization condition $u^\mu u_\mu = -1$, the dot refers to the derivative over a proper time τ . The electromagnetic tensor given by $F_{\mu\nu} = A_{\nu,\mu} - A_{\mu,\nu}$ and highlighting its antisymmetric nature.

3.2 Charged particle dynamics: Hamiltonian and effective potential

The dynamics of a charged particle around a BH with CDM located within a uniform magnetic field can be conveniently explained using the Hamiltonian formalism [36]. The general form of the Hamiltonian is given by

$$H = \frac{1}{2} g^{\alpha\beta} (\pi_\alpha - qA_\alpha) (\pi_\beta - qA_\beta) + \frac{1}{2} m^2 \quad (24)$$

where $g^{\alpha\beta}$ are the components of the inverse metric tensor, corresponding to the modified Schwarzschild metric introduced in Eq.(1) and Eq.(15). The quantity π_α represents the generalized (canonical) four-momentum, which linked to the kinetic four-momentum $p^\alpha = mu^\alpha$ by

$$\pi^\mu = p^\mu + qA^\mu, \quad (25)$$

with u^α denoting the particle's four-velocity. Constructing the effective potential from the Hamiltonian formalism is crucial to understanding the trajectory of charged particles in the vicinity of magnetized BHs. This topic has been extensively studied in the literature; see, for example, Refs. [36, 57, 58]. In the framework of this study, we specifically concentrate on the behavior of charged particles around a non-rotating, uncharged BH surrounded by a CDM halo and operating within a uniform magnetic field.

The Hamiltonian equations of motion are given by

$$m \frac{dx^\mu}{d\tau} = p^\mu = \frac{\partial H}{\partial \pi_\mu}, \quad \frac{d\pi_\mu}{d\tau} = -\frac{\partial H}{\partial x^\mu}. \quad (26)$$

Applying Eq.(25), conserved quantities corresponding to the spacetime symmetries are obtained. The energy E and axial angular momentum L of a particle are given by

$$E = -\pi_t = g_{tt}(mu^t + qA^t) = mg_{tt}\dot{t}, \quad (27)$$

$$L = \pi_\phi = mg_{\phi\phi} \left(\dot{\phi} + \frac{qB}{2m} \right). \quad (28)$$

The remaining components of the motion are governed by

$$\dot{r} = g^{rr} p_r \quad \text{and} \quad \dot{\theta} = g^{\theta\theta} p_\theta. \quad (29)$$

The dynamical equation governs charged particles motion in Cartesian coordinates (x, y, z) can be derived through coordinate transformation.

$$x = r \cos \phi \sin \theta, \quad y = r \sin \phi \sin \theta, \quad z = r \cos \theta. \quad (30)$$

Finally, it is convenient to define the specific (per unit mass) quantities [59]

$$E' = \frac{E}{m}, \quad L' = \frac{L}{m}, \quad B' = \frac{qB}{2m}. \quad (31)$$

The Hamiltonian given in Eq.(24) can be rewritten as represented below

$$H = \frac{1}{2} g^{rr} p_r^2 + \frac{1}{2} g^{\theta\theta} p_\theta^2 + \frac{1}{2} m^2 g^{tt} [V_{\text{eff}}(r, \theta) - E'^2] \quad (32)$$

where $V_{\text{eff}}(r, \theta; L', B', \kappa)$ indicates the effective potential, defined as

$$V_{\text{eff}}(r, \theta; L', B', \kappa) \equiv g_{tt} \left[1 + \left(\frac{L'}{r \sin \theta} - B' r \sin \theta \right)^2 \right]. \quad (33)$$

The term enclosed in parentheses represents the central force enhancement of the effective potential, arising from the combined effects of B' and L' .

Moreover, the system exhibits a double parity symmetry under the following transformation:

$$(L', B') \leftrightarrow (-L', -B'), \quad (34)$$

The symmetry equation indicates that both L' and B' may have either positive or negative sign. The angular momentum sign L' determines the direction of the charged particle trajectory around the BH: A positive (negative) L' corresponds to a counterclockwise (clockwise) motion viewed from above the BH. Similarly, the sign of B' indicates the orientation of the magnetic field vector \vec{B}' , with a positive (negative) B' pointing upward (downward) along the z -axis. The analysis of V_{eff} provides essential information that complements the solution of the equations of motion for charged particles [36, 57]. When L' and B' share the same sign, the resulting Lorentz force acts repulsively on the charged particle. In contrast, if L' and B' have opposite signs, the Lorentz force becomes attractive. Moreover, the movement of charged particles is constrained by energy conservation, where turning points occur under the condition $p_r = p_\theta = H = 0$. In this sense, V_{eff} satisfies

$$E'^2 = V_{\text{eff}}(r, \theta; L', B', \kappa). \quad (35)$$

The variation of the effective potential in the presence of a uniform magnetic field, which incorporates the effects of CDM, is illustrated in Fig. 2. The results are presented for angular momentum $L' = 11$ with $B' > 0$, $B' < 0$ in a vanishing $B' = 0$.

It is observed that the magnetic field significantly affects the V_{eff} at large distances from the BH. However, near the event horizon, gravitational effects dominate over the magnetic influence in the equatorial plane $\theta = \pi/2$. More specifically, as the parameter κ increases at a fixed characteristic radius R_s , the gravitational pull becomes more stronger, leading to a suppression of B' influence close to the event horizon. The dark region in Fig. 2, bounded by the dashed black line, represents the stability region for charged particle orbits. The impact of CDM is visible as this stable region shifts toward the BH, indicating that charged particles are increasingly trapped closer to the event horizon. Furthermore, the event horizon radius itself increases with higher values of κ , as previously discussed in Sec. 2 and shown in Fig. 1. In the cases of $B' = \pm 0.1$, the stability region acquires a parabolic form, reflecting the balance between gravitational attraction and magnetic repulsion in this scheme. In addition, positive magnetic field values produce a larger stability region compared to negative values.

A fundamental property of the BH background under consideration is its axial symmetry. In the presence of both a gravitational field and an external uniform magnetic field, the spacetime remains invariant under rotations about the symmetry axis. As a result, V_{eff} governing the path of charged particles is independent of the azimuthal coordinate ϕ . This symmetry significantly simplifies the analysis, allowing V_{eff} to be treated as a two-dimensional function $V_{\text{eff}}(r, \theta)$. Alternatively, it can be represented using spherical coordinates (x, z) , defined in Eq. (30), which are particularly convenient for visual representation and numerical evaluation. The structure and behavior of the effective potential in this reduced configuration space are clearly illustrated in the lower panels of Fig. 2, highlighting the role of symmetry in constraining the dynamics of charged particles in such a background. Our investigation focuses on understanding how the presence of a CDM halo, in conjunction with a uniform magnetic field, influences the effective potential. Parameters κ , which characterize the density profile of the CDM distribution, have a

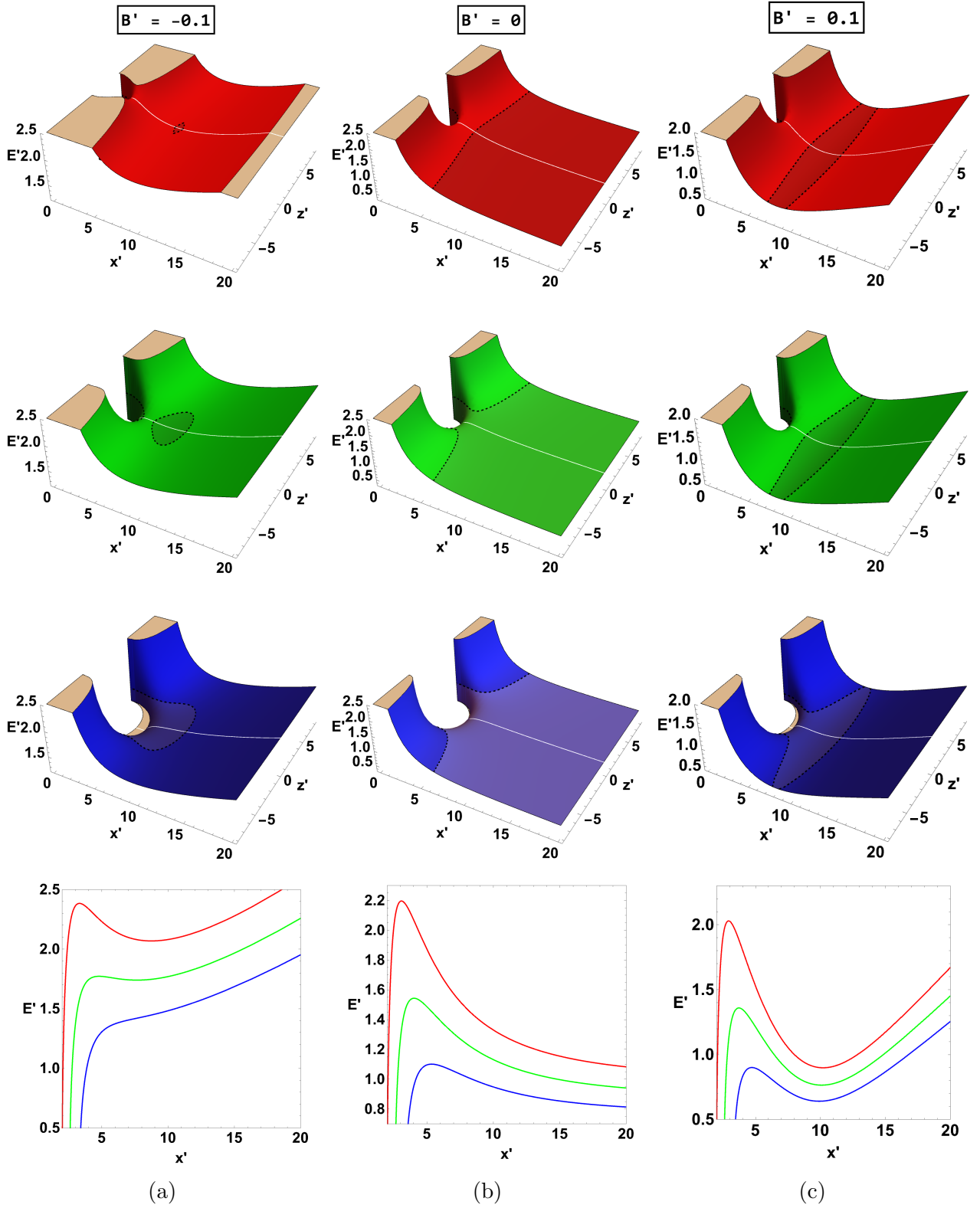


Figure 2: The effective potential in the equatorial plane is shown for various values of κ and magnetic field strength $B' = 0, \pm 0.1$. The first row corresponds to $\kappa = 0$, the second row to $\kappa = 10$, and the third row to $\kappa = 20$. The fourth row presents a two-dimensional projection at $z' = 0$. The first three rows display three-dimensional representations of the effective potential, while the fourth row provides a comparative 2D slice for fixed angular momentum $L' = 11$.

significant impact on shaping the spacetime geometry and consequently the effective potential experienced by charged particles. Notably, the effective potential exhibits distinct regions: a negative branch located within the BH interior and a positive branch outside the event hori-

zon. The crossover between these two regimes occurs precisely at the event horizon, which acts as a natural boundary separating the interior and exterior dynamics. As illustrated in Fig.1, the the event horizon radius is strongly influenced by the parameter κ . For example, where $\kappa = 0$, V_{eff} is zero at $r = 2$, positive for $r > 2$, and negative for $r < 2$, consistent trough the classical Schwarzschild solution. However, when CDM is included—for example, with $\kappa = 10$ and $R_s = 1000$ the event horizon shifts outward. In this case, the effective potential is negative for $r < 2.57063$, positive for $r > 2.57063$, and vanishes at $r \approx 2.57063$. This shift indicates that the gravitational influence of the CDM halo modifies the BH's causal structure. Therefore, our analysis of the V_{eff} is restricted to the event horizon exterior region, where stable orbits and observationally relevant dynamics occur.

The stationary points of the V_{eff} that govern the orbital motion of charged particles around a BH subjected to a uniform magnetic field and surrounded by CDM are determined. by solving the following equations:

$$\partial_{\{r,\theta\}} V_{\text{eff}}(r, \theta, L', B', \kappa) = 0. \quad (36)$$

All extrema of the effective potential for charged particle dynamics in the equatorial plane of a Schwarzschild BH wrapped in a uniform magnetic field—also surrounded by a CDM halo—are located in that same plane associated with $\theta = \pi/2$, as shown in [36]. The other extremum corresponds to the radial coordinate r , which satisfies the condition for stationary orbits.

$$L'^2 ((r + R_s)\mathcal{G} + \mathcal{N}) - 2L'B'r^2\mathcal{N} - B'^2r^4(r + R_s)\mathcal{G} + (r^2 + B'^2r^4)\mathcal{N} = 0. \quad (37)$$

where the function G denotes

$$\mathcal{G}(r, \kappa, R_s) = 2M - r\mathcal{T}^{-1}, \quad (38)$$

and \mathcal{N} stands for

$$\mathcal{N}(r, \kappa, R_s) = M(r + R_s) - 4\kappa\pi\mathcal{T}^{-1} \left(r - (r + R_s) \ln \left[\frac{r + R_s}{R_s} \right] \right). \quad (39)$$

Where the \mathcal{T} encoded the DM term as

$$\mathcal{T} = \left(\frac{1}{R_s}(r + R_s) \right)^{\frac{8\kappa\pi}{r}} \quad (40)$$

Since the above equation is of the fifth order in r , it may admit more than five roots, corresponding to multiple extremal points. By treating Eq.(37) as a second-degree equation expressed with respect to the L' , one can straightforwardly derive the solution. Specifically, we obtain:

$$L'_{\pm}(r; B', \kappa, R_s) = \frac{B'\mathcal{N}r^2 - \frac{1}{2}\sqrt{4B'^2\mathcal{N}^2r^4 - 4(\mathcal{G}(r + R_s) + \mathcal{N})((B' + 1)\mathcal{N}r^2 - B'^2\mathcal{G}r^4(r + R_s))}}{\mathcal{G}(r + R_s) + \mathcal{N}} \quad (41)$$

The positive root of Eq.(41) corresponds to configurations with either stable or unstable circular orbits, whereas the negative root is associated via the maxima of the V_{eff} , indicating regions of instability. Furthermore, the V_{eff} maxima and minima can be identified by analyzing its second derivative with respect to the r . These extremal points provide key insights into the radial positions, E' , and L' associated with particle trajectories. In particular, the condition for the ISCO is evaluated by the inflection point, defined by $\partial_r^2 V_{\text{eff}} = 0$. Solving this condition yields

$$L'_{\text{ex}}(r; B', \kappa, R_s) = \frac{2B'\mathcal{N}r \pm \sqrt{-2\mathcal{G}\mathcal{N}r + 4B'^2\mathcal{N}^2r^2 - 4B'^2\mathcal{G}\mathcal{N}r^3 + 5B'^2\mathcal{G}^2r^4 + 4B'^2\mathcal{G}^2r^3R_s}}{\mathcal{G}}. \quad (42)$$

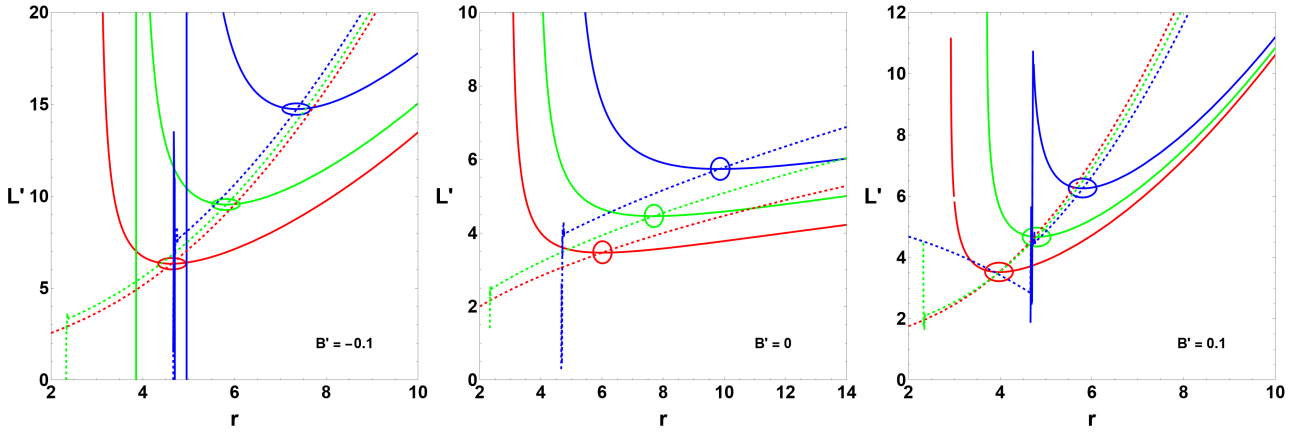


Figure 3: Angular momentum in function of radii L_{\pm} (thick), L'_{ex} (dashed), $\kappa = 0$ (red), $\kappa = 10$ (blue), $\kappa = 20$ (green), within several values of B' . Circles representing the point of intersection of L_{\pm} and L'_{ex} indicating the ISCO position.

Fig.3 illustrates the circular orbits of charged particles in space-time influenced by CDM and a magnetic field.

The extrema of the functions $L_{\pm}(r)$ correspond to the local extrema of the effective potential in the equatorial plane. The dashed curves in the figure represent these extremal values, denoted by $L'_{ex}(r)$, which help identify the stability characteristics of the orbits. The point where the solid and dashed curves intersect in Fig.3 marks the ISCO positions. The location of the ISCO is not universal but instead varies through the merged influence of B' and the CDM halo. Circular orbits remain stable for radial distances $r > r_{\text{ISCO}}$, whereas they become unstable for $r < r_{\text{ISCO}}$. The extent and position of these regions are directly affected through the strength and distribution of the surrounding DM.

Specifically, the ISCO radius is established by the intersection of the functions $L'_{ex}(r)$ and $L'_{\pm}(r)$. To analyze how the magnetic field and CDM affect the ISCO location, a detailed representation is provided in Fig.4. The plot demonstrates that the parameter κ , which characterizes

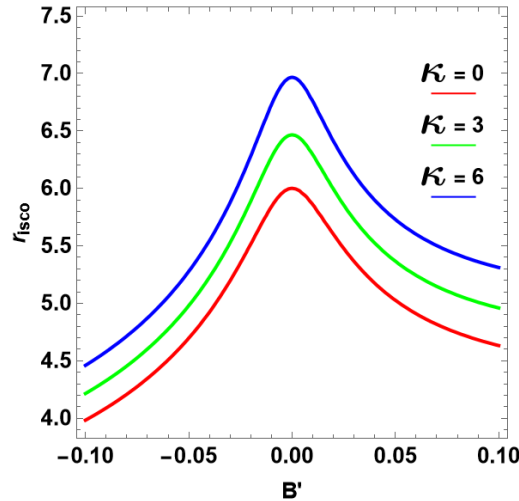


Figure 4: ISCO radius variation on function of magnetic field B' in different values of κ .

the density of the CDM halo, alongside with B' , has a significant impact of the ISCO radius. Interestingly, the magnetic field and CDM exert opposing effects: an increase in the magnitude of B' regardless of its sign—tends to shift the ISCO inward, closer to the event horizon, whereas an increase in κ pushes the ISCO outward, farther from the BH event horizon.

At large distances $r \rightarrow \infty$ and near the equatorial plane $\theta \approx \pi/2$, the path of a charged

particle in a uniform magnetic field becomes radially confined. This confinement arises from the $B'r^2$ term in the effective potential, as seen in Eq.(33), which acts as a dominant repulsive barrier in the radial direction.

Under the circumstances of a repulsive Lorentz force, the effective energy boundaries open along the polar direction, permitting particles with ($q \neq 0$) move off to infinity following the z -axis. In contrast, when the Lorentz force is attractive, it drives the particle into a spiraling trajectory, curving inward toward the BH.

Therefore, the requirement for a charged particle to move toward infinity, in the case where $B' \geq 0$, can be expressed as follows:

$$E'_{\min} \geq \sqrt{\left(1 - \frac{2}{r}(1 + \kappa\pi \ln \frac{r}{R_s})\right)}. \quad (43)$$

Reflecting the lowest of the energy of the particle at the infinity. In the case of $B' < 0$, the energetic condition of the particle asymptotically approach infinity to the following form:

$$E'_{\min}(\kappa, R_s; B', L') \geq \sqrt{\left(1 - \frac{2}{r}(1 + \kappa\pi \ln \frac{r}{R_s})\right)} (1 - 4B'L'). \quad (44)$$

From Eqs.(43) and (44), one can deduce the conditions under which charged particles become trapped around a magnetized BH surrounded by a CDM halo. In particular, the minimum energy E'_{\min} required for trapping is influenced by the distribution of CDM. This effect becomes increasingly significant as the CDM density intensifies, highlighting the role of the halo in shaping the energy landscape of particle motion. These bound states arise when the particle's specific energy satisfies the equality $E' = E'_{\min}$. Oscillatory trapped motion of charged particles is therefore permitted as long as the following condition is fulfilled

$$L'_1 < L' < L'_2. \quad (45)$$

In the case where $B' \geq 0$, the behavior of oscillating charged particles in trapped states is governed by the expression stated below for the specific angular momentum $L'_{1,2}$:

$$L'_{1,2} = \frac{r \left(B'r(-r + 2\mathcal{T}) \pm \mathcal{T} \sqrt{(2 - r\mathcal{T})(-2 + r(-1 + \mathcal{T}))} \right)}{2\mathcal{T} - r}. \quad (46)$$

whereas for $B' < 0$, the corresponding condition for trapped states is outlined by:

$$L'_{1,2} = \frac{r \left(B'r(-2 + r(-2 + \mathcal{T})) \pm \sqrt{(2 + r(1 + \mathcal{T}))(-2 + r(4B'^2r^2 + \mathcal{T}))} \right)}{r\mathcal{T} - 2}. \quad (47)$$

In both expressions, the function \mathcal{T} encodes the influence of the CDM halo and is defined as: $\mathcal{T} = \left(\frac{1}{R_s}(r + R_s) \right)^{\frac{8\kappa\pi}{r}}$. These quantities characterize the angular momentum bounds required for the existence of stable, bounded oscillatory trajectory in the surroundings of a magnetized BH embedded in a CDM environment.

Having discussed the extrema of Eq.(41) with respect to the coordinate r , we now turn to the behavior of the effective potential described by L' . Fig.5 illustrates the local extrema of V_{eff} for various values of the intensity of the B' , highlighting how these features vary with changes in the DM parameter κ relative to R_s .

The point at which the potential curve deviates sharply corresponds to the specific energy at the ISCO, E'_{ISCO} . The plot demonstrates that increasing κ contributes to a decrease in V_{eff} associated via the ISCO, reflecting the influence of the CDM halo.

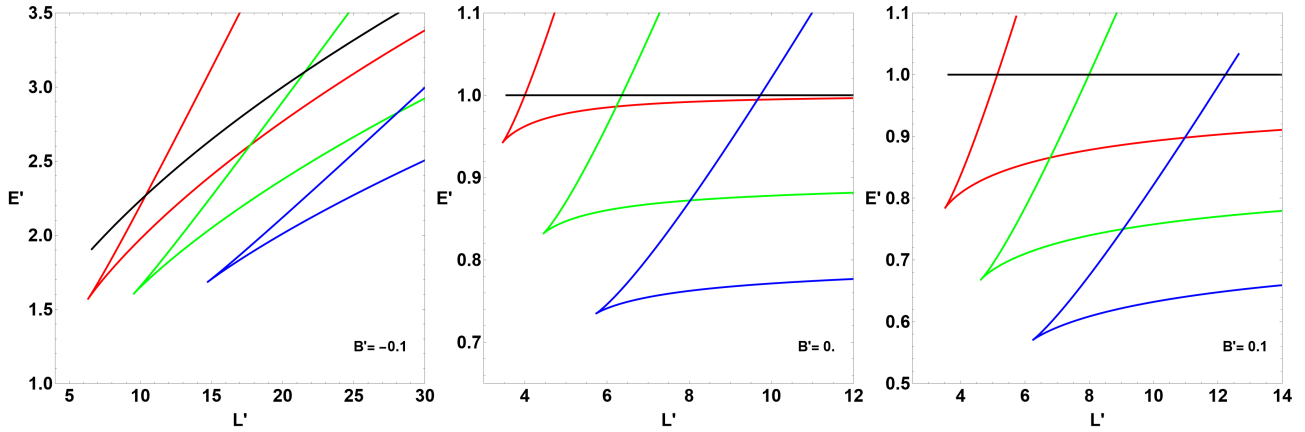


Figure 5: Energy plotted against of angular momentum for distinct values of κ : $\kappa = 0$ (red), $\kappa = 10$ (green), and $\kappa = 20$ (blue). The black curve represents the minimum energy required for a particle tend to infinity, shown for multiple values of B' .

The minimal energy configuration required for a particle to diverge to infinity is indicated by the thick black line in the Fig.5. This line separates the curves into two distinct regions that correspond to the local minima and maxima of V_{eff} . The region below the black line represents bound states, indicating where trapped particle motion is possible. In particular, the extent of this region increases with larger values of κ , demonstrating the growing consequence of the CDM halo on the confining trajectories of particles.

the contribution of the CDM halo on the development of L' and E' is further illustrated in Figs.6 and 7, where its effect on the trajectories of charged particles is explicitly analyzed

In fact, with regard to a negative uniform magnetic field with strength $B' = -0.1$ is illustrated in Fig.6, while the corresponding case for a positive field $B' = 0.1$ is shown in Fig.7.

From panels (a), one can notice that the $(x - y)$ plot displays the orbital trajectories of charged particles projected onto the equatorial plane. The color-coded trajectories linked to increasing values of the CDM density parameter $\kappa = 0$ (red), 10 (green), and 20 (blue), with all other parameters held constant: $R_0 = 8.1$, $L' = 15$, and $B' = -0.1$. As κ increases, the orbits become more confined, indicating stronger gravitational effects due to the denser dark-matter halo. The red trajectory ($\kappa = 0$) shows the widest orbit, gradually transitioning to more tightly bound orbits for green and blue as the influence of CDM intensifies.

The $(x - z)$ plane shows the vertical (out-of-plane) extension of the particle motion. Equipotential contours (dashed lines) are included, which delineate the effective energy boundaries governing motion in the poloidal plane. The escape trajectories for ($\kappa = 0$) and 10 are open, allowing the particles to exit along the z -axis, while for $\kappa = 20$, the particle appears trapped within the potential well. The right panel offers a three-dimensional visualization of the trajectories for different κ , clearly showing how the presence of CDM modifies the spatial extent and structure of the motion. The shrinking of the orbit's spatial envelope from red to blue confirms that CDM increases gravitational confinement of trajectories.

The (b) panels mirror the structure of (a), but under a different parameter set: $R_0 = 9.5$, $L' = 11$, and the same $B' = -0.1$. The previously observed behavior in $(x - y)$ plane persist, but the initial orbits begin closer to the BH, and the confining contribution of CDM is more pronounced even at lower κ . The $(x - z)$ plane confirms the transition from open to closed energy surfaces as κ grows, with the particle at $\kappa = 20$ exhibiting a clear bound state within the polar confinement zone. Lastly, the 3D visualization reinforces the conclusion that CDM density plays a major role in spatially restricting particle motion. The orbits shrink progressively as κ increases, with tighter confinement around the BH.

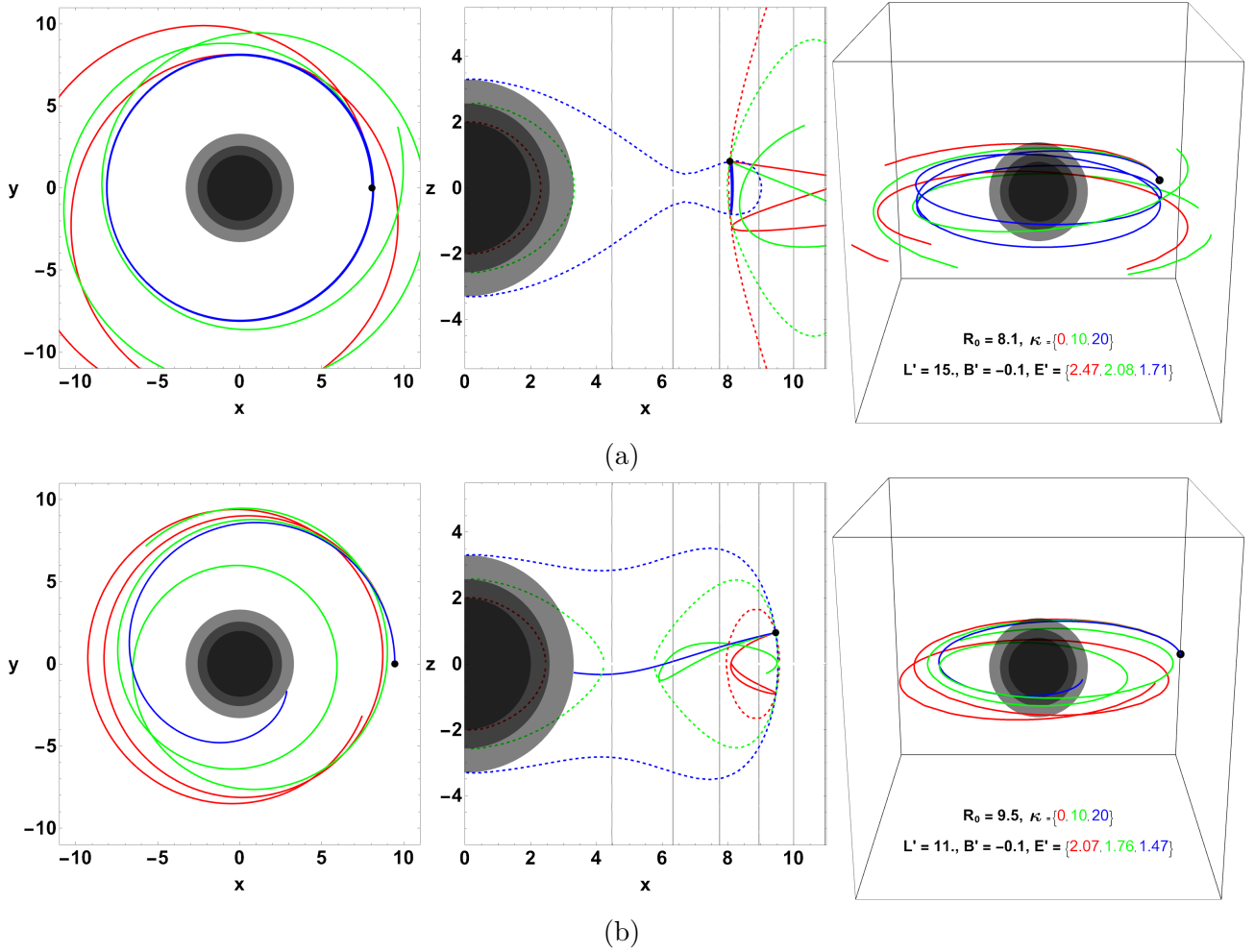


Figure 6: *Illustration of charged particle trajectories for different values of κ around BH embedded in a uniform magnetic field of strength $B' = -0.1$ and CDM halo. Parameters R_0 , L' and E' present initial position, angular momentum and specific energy of charged particle respectively. The disks at the centers of the panels in the first and second rows represent the BH event horizon for varying κ , while in the third row, the horizons are depicted as spherical objects. Panel (a) highlights the variation of the ISCO radius with increasing κ , and panel (b) illustrates the effect of the CDM halo on particle dynamics. Notably, a trapped state appears for $\kappa = 20$, indicating the growing influence of CDM in confining particle motion.*

The fig.7 which illustrates the particle dynamics within a positive uniform magnetic field $B' = 0.1$, with the same angular momentum $L' = 7$ used for all trajectories.

The trajectories exhibit more extended and less confined motion, particularly in the $(x - z)$ planes and 3D views. Higher CDM values continue to influence the degree of curvature, effectively trapping particles. This effect is clearly illustrated in the case where $\kappa = 20$. Furthermore, In panel (b), the red and green trajectories (lower κ) display complex looping structures in the $(x - y)$ plane, driven by magnetic effects, which are more pronounced than in the $B' < 0$ depicted in Fig.6.

Rigorously speaking, CDM, characterized by the parameter κ , significantly perturbs the coordinate of the ISCO and alters E' of charged particles, regardless of the magnetic field's sign. As shown in the figures, increasing κ enhances the likelihood of particles becoming trapped in bounded orbits. These trapped states are defined by inner and outer energy boundaries, which confine the motion to a finite radial region. However, at sufficiently high CDM density, the confinement may break down, causing particles to spiral inward toward the BH.

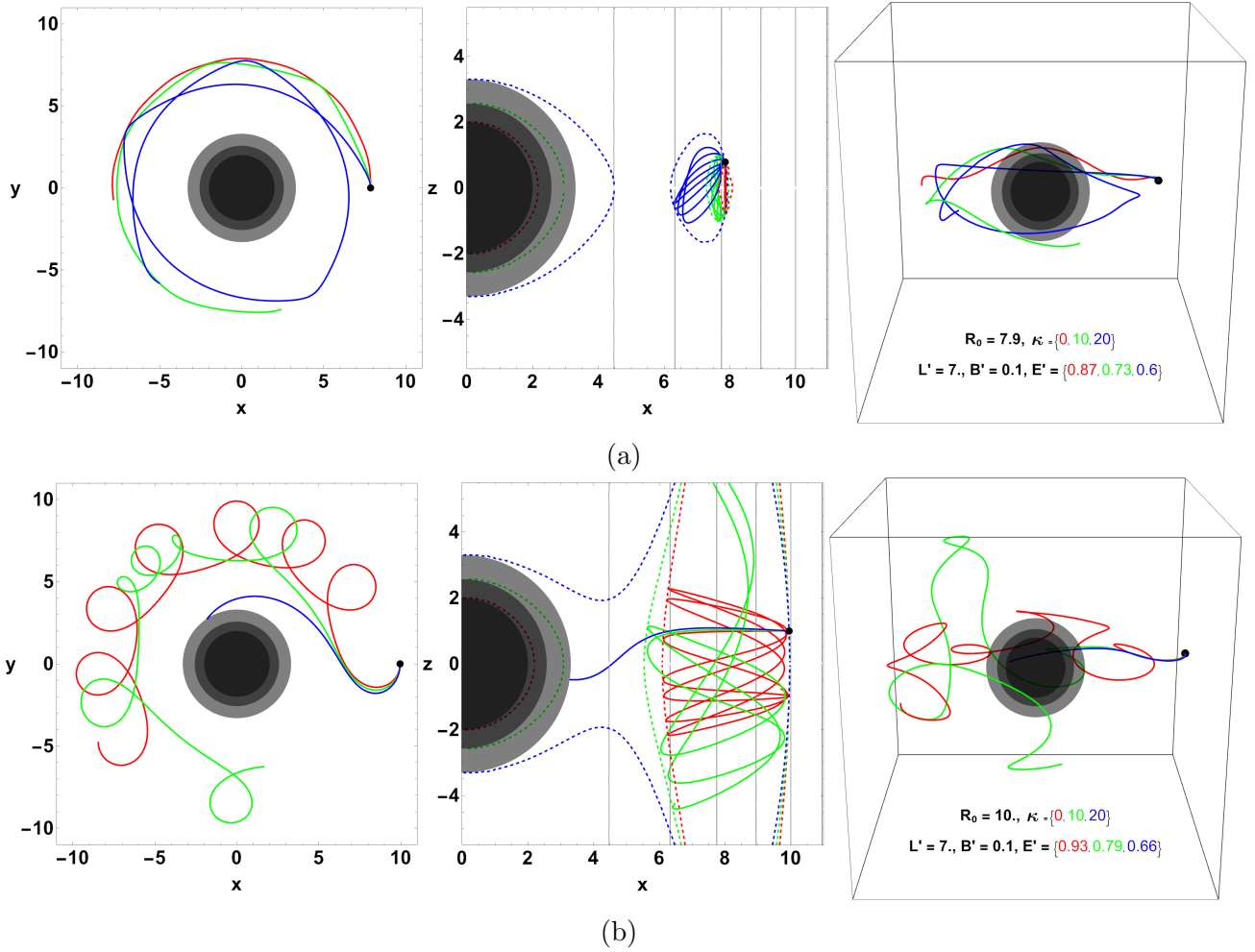


Figure 7: Charged particle trajectories for different values of κ around BH surrounded by a uniform magnetic field of strength $B' = 0.1$ and CDM halo. Parameters R_0 , L' and E' present initial position, angular momentum and specific energy of charged particle respectively. The disks at the centers of the panels in the first and second rows represent the BH event horizon for varying κ , while in the third row, the horizons are depicted as spherical objects. Panel (a) isco located where $\kappa = 0$, for (b) charged particles trajectories for $\kappa = 20$ trapped toward BH, while for decreasing values of κ particles trajectories orbiting in a curled trajectories while it variate and become large where κ value close to zero.

3.3 More on curled trajectories

The conserved angular momentum associated with the axial symmetry of the charged particle's trajectory is expressed in the following expression

$$\dot{\phi} = \frac{L'}{r^2} - B'. \quad (48)$$

For $B' = 0$, with $L' > 0$ and $r > 0$, the axial coordinate ϕ increases, indicating standard prograde motion. However, when $B' > 0$, ϕ may decrease, implying a reversal in the azimuthal direction. This behavior results in curled or spirallike trajectories, as the Lorentz force modifies the particle's angular motion around the BH. The condition for the occurrence of curled trajectories can be derived from the angular momentum constraint, which must satisfy:

$$L'(r; B') \geq B'r^2. \quad (49)$$

This inequality leads to the corresponding condition on the specific energy required for such spiral motion, expressed as

$$E'(\kappa, R_s; B', L') > \sqrt{-\frac{2}{\sqrt{\frac{L'}{B'}}} + \left(1 + \frac{\sqrt{\frac{L'}{B'}}}{R_s}\right)^{-\frac{1}{\sqrt{\frac{L'}{B'}}} 8\kappa\pi}}. \quad (50)$$

Curled trajectories are clearly illustrated in Fig.7, where different initial radii are considered under the same angular momentum and magnetic field strength. As the DM parameter κ augmentation, the curvature of the trajectories becomes more significant, and the spatial extent of the curls gradually diminishes, indicating stronger gravitational confinement induced by the CDM halo.

4 Harmonic oscillations of a charged particle in a magnetized BH with CDM halos

A charged particle in equilibrium is sited at the ISCO, at a radius denoted by r_{ISCO} , immediately beyond the BH's event horizon. At this position, the particle reveals stable circular motion corresponding to the minimum of V_{eff} in $\theta = \pi/2$. When the particle experiences a very small displacement from this equilibrium point, it undergoes oscillatory motion around the potential minimum.

To describe such harmonic oscillations, we analyze small perturbations along both the radial and the latitudinal directions. These are represented by $r = r_{\text{ISCO}} + \delta$ and $\theta = \theta_{\text{ISCO}} + \delta$, corresponding respectively to horizontal (radial) and vertical (latitudinal) perturbations. The dynamics of these oscillations are regulated by the following equations

$$\ddot{\delta i} + w_i^2 \delta i = 0. \quad (51)$$

Here, $i = (r, \theta)$, and the double dot denotes the second derivative as regards the particle's proper time τ . The quantities ω_r and ω_θ represent the radial and latitudinal oscillation frequencies, respectively. In the context of a BH spacetime influenced by gravity, a magnetic field, and a surrounding DM halo, the corresponding frequencies can be computed using the following expression

$$\omega_r^2 = \frac{\partial^2 V_{\text{eff}}}{\partial r^2}, \quad \omega_\theta^2 = \frac{1}{r^2 f(r)} \frac{\partial^2 V_{\text{eff}}}{\partial \theta^2}. \quad (52)$$

In addition, two other important frequencies arise: the Keplerian frequency ω_ϕ and the Larmor frequency ω_L [36]. The Keplerian frequency ω_ϕ characterizes the angular (azimuthal) motion of the particle, while the Larmor frequency ω_L describes its circular motion induced by the uniform magnetic field. These frequencies are given by

$$w_\phi = \frac{d\phi}{d\tau}, \quad w_L = \frac{qB}{m} = 2|B'|. \quad (53)$$

The Larmor frequency w_L is unrelated to the radial coordinate, and its effect becomes increasingly dominant at extended range from the BH, where the uniform magnetic field plays a more significant role.

Finally, the radial, latitudinal, and Keplerian frequencies can be defined as follows [37]

$$w_r = \sqrt{\left(B'^2 + \frac{3L'^2}{r^4}\right) f(r) + \frac{(r^2 + (L' - B'r^2)^2) (f'(r))^2}{r^2 f(r)} - \frac{(r^2 + (L' - B'r^2)^2) f''(r)}{2r^2}}, \quad (54)$$

$$\omega_\theta = \sqrt{-B'^2 + \frac{L'^2}{r^4}}, \quad (55)$$

$$\omega_\phi = \frac{L'}{r^2} - B'. \quad (56)$$

In all expressions for the characteristic frequencies, L' is set to L'_+ , as defined in Eq.(41). Fig.8 illustrates the behavior of the fundamental frequencies-radial (ω_r), latitudinal (ω_θ), Keplerian (ω_ϕ), and Larmor (ω_L) as functions of r .

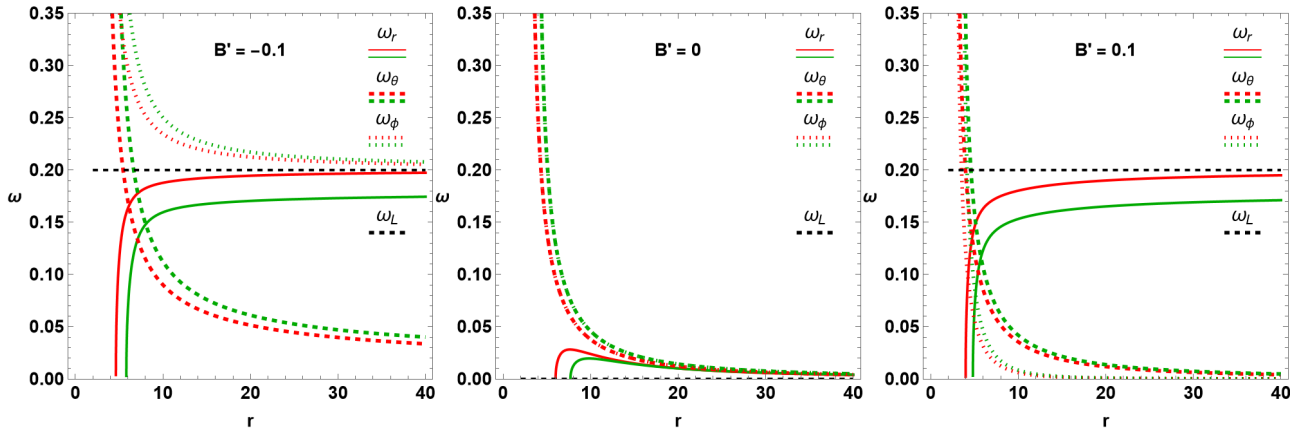


Figure 8: Fundamental frequencies ω_r (Thick line), ω_θ (Dashed line), ω_ϕ (Dotted line) and ω_L (black dashed line), on function of radii where $\kappa = 0$ (Red) $\kappa = 10$ (Green) within $R_s = 1000$, for different values of B' .

The ratios between these frequencies provide important insights into the dynamics and geometry of charged particle motion around a BH immersed in a uniform magnetic field and surrounded by a DM halo. In particular, these ratios can be used to estimate the shape and nature of the particle trajectories.

The comparison of these fundamental frequencies is presented in this figure for three distinct cases: $B' = 0$, and in the presence of both positive and negative magnetic fields ($B' = \pm 0.1$). Additionally, the figure explores how the charged particle orbits behave for a given CDM density parameter κ . As previously discussed, gravitational effects dominate near the BH (at small radii), whereas the magnetic field becomes more influential at larger distances. This behavior is also reflected in the frequency profiles. The Red thick and dashed lines represent the frequencies in the presence of the magnetic field alone (i.e., $\kappa = 0$), consistent with results in [36]. In contrast, our case with $\kappa > 0$ is illustrated by Green (lines, dashed, dotted), showing the modifications induced by the dark-matter halo.

According to Newtonian gravity, all characteristic frequencies are identical ($\omega_r = \omega_\theta = \omega_\phi$), which corresponds to charged particles following elliptical trajectories. This Newtonian behavior is plotted in the leftmost panel of Fig.8. The trajectory of charged particles is notably affected by the presence of a uniform magnetic field, regardless of its sign. For $B' > 0$, the Keplerian frequency ω_ϕ approaches the Larmor frequency ω_L (represented by the dashed black line in Fig.8) from above at large distances. In contrast, when $B' < 0$, the frequencies ω_ϕ and ω_θ become nearly identical at large distances from the ISCO radius (where $\omega_r = 0$), and

both asymptotically approach zero. The influence of the CDM halo is most significant in the inner region near r_{ISCO} , where it affects both ω_θ and ω_ϕ . However, at large distances, the effect diminishes, and the frequency profiles converge, showing little difference between cases $\kappa = 0$ and $\kappa = 10$.

The fundamental frequencies can be translated into the corresponding frequencies as measured by distant observers located at spatial infinity. These observed frequencies are given by

$$\nu_i = \frac{c^3}{2\pi GM} \frac{\omega_i}{-g^{tt}E'} \quad (57)$$

where $i = \{r, \theta, \phi\}$, G and c denote the gravitational constant and the speed of light, respectively. The factor $(-g^{tt}E')^{-1}$ accounts for the gravitational redshift experienced by the particle.

In Fig.9 we depict the outcome of the CDM parameter—density κ on the fundamental frequencies (radial, latitudinal, and Keplerian) of a charged particle orbiting a BH situated within a uniform magnetic field and DM halo as measured by distant observers located at spatial infinity. The behavior is shown for three different magnetic field strengths: $B' = 0, \pm 0.1$.

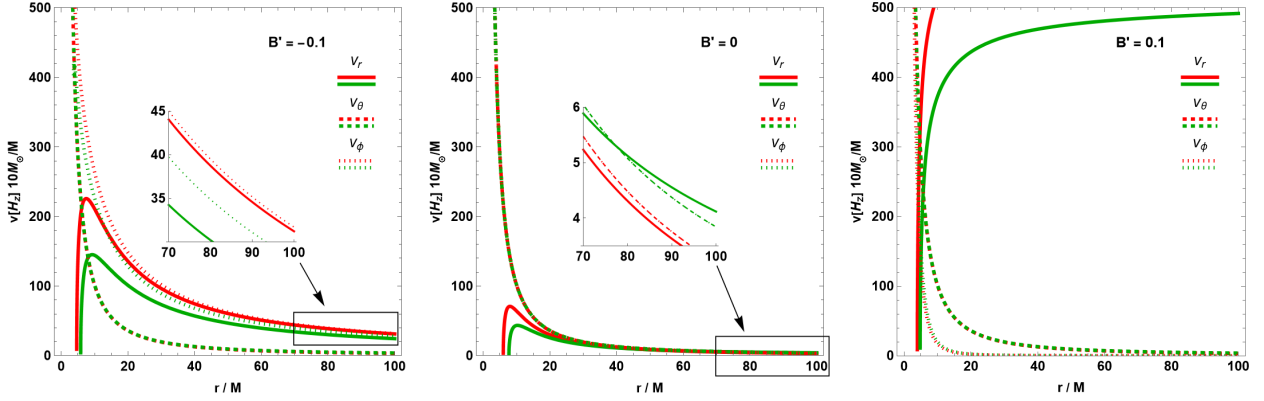


Figure 9: Fundamental frequencies ν_r (Thick), ν_θ (Dashed), ν_ϕ (Dotted) as measured by distant observers located at spatial infinity for different values of κ , 0 (Red), 10 (Green), for different values of B' .

Green lines correspond to the case $\kappa = 10$, while red lines represent the scenario with no DM contribution, i.e., $\kappa = 0$. The presence of CDM leads to a reduction in the charged particle motion frequencies across all values of B' . In the case of $B' < 0$, and for $\kappa = 0$, the radial frequency ν_r and the Keplerian frequency ν_ϕ converge at large distances. As κ increases, the gap between ν_r and ν_ϕ becomes more pronounced. In addition, for $B' = 0$, and for $\kappa = 10$, we observe an intersection between ν_r and ν_ϕ at large distances, where the radial frequency lies above the Keplerian frequency.

4.1 Ionized particles and jet particles

Jet particles (e.g., electrons, protons, and positrons) are a well-known phenomenon correlated through the presence of strong B' near BHs. These particles are typically launched from the innermost regions of the accretion disk, which features a mixture of hot gas and dust spiraling around the BH. The mechanism behind their acceleration is primarily driven by an intense repulsive Lorentz force resulting from the interaction between particle with $q \neq 0$ and B' . As a result, ionized particles can be accelerated to relativistic speeds, traveling nearly at the speed of light along magnetic field lines into vacuum space. These high-energy outflows, or relativistic

jets, are of fundamental importance in probing the physical conditions near compact objects. Their detection provides valuable insights into the structure of the surrounding spacetime, the configuration of magnetic fields, and the luminosity profile of the central object.

Next, we will examine the dynamics of jet particles in the region surrounding a BH interacting with a strong uniform magnetic field and surrounded by a CDM halo. Fig.10 reveals the effect of $B' = 1$ on the trajectories of ionized particles, for discrete values of the CDM density parameter κ . The characteristic radius R_s is kept fixed in all cases to isolate the impact of varying the density of CDM.

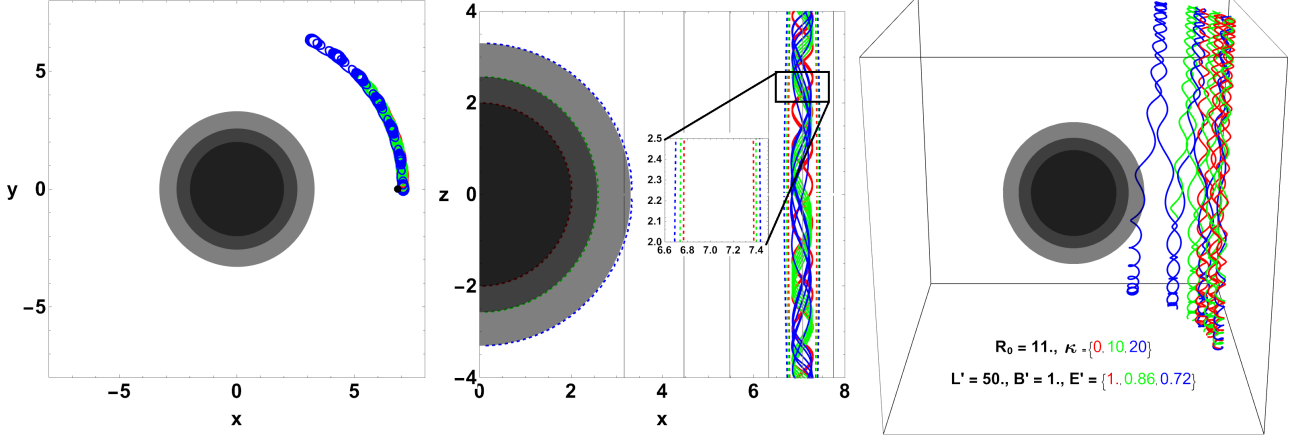


Figure 10: Trajectories of ionized charged particles for different values of the CDM density parameter κ , around a BH immersed in a strong, positive uniform magnetic field of strength $B' = 1$.

The setup specifically considers off-equatorial motion in a spacetime environment influenced by a CDM halo. The second column displays the specific energy E' associated with each κ scenario, while the middle zoom shows the corresponding energetic boundaries of charged particles, defined by the effective potential (dashed lines). The central disks in the left and middle columns indicate the locations of the BH horizons for different values of κ . The rightmost column provides a 3D visualization of the system, providing improved clarity of the geometric configuration and particle dynamics.

The results demonstrate that increasing the CDM density parameter κ significantly alters the structure of the confinement and acceleration zones, thereby modifying the particle trajectories and escape behavior of jet-like particles. Concretely, it is obvious that the trajectories of the particles are predominantly directed along the z axis. According to the escape condition discussed in Eq.(43), only the particle in case $\kappa = 0$ shown as the red trajectory possesses sufficient energy to escape to infinity. As κ increases, the specific energy associated through the trajectory of the particle decreases, indicating that the contribution of the CDM halo becomes dominant over the magnetic field in the near horizon region. Furthermore, the energy boundaries expand with increasing κ , implying a deeper potential well and stronger confinement.

Throughout Fig.11, we plot the power spectral densities (PSD) corresponding to the radial, latitudinal, and Keplerian coordinates. These spectra are derived from the trajectories of particles with charge orbiting a BH immersed in a strong uniform magnetic distribution and surrounded by a CDM halo. The dashed lines refers the peak positions of the fundamental frequencies of particle motion near circular orbits, as computed from Eqs.(54)–(56).

The panel (a) corresponds to a particle with $E' \geq 1$, escaping to infinity, consistent with Eq.(43). As the CDM density parameter κ increases (panels b–c), the PSD structure changes significantly. For high κ (panel c), the radial frequency dominates while latitudinal and Keplerian components are suppressed, indicating stronger confinement and increased dynamical complexity.

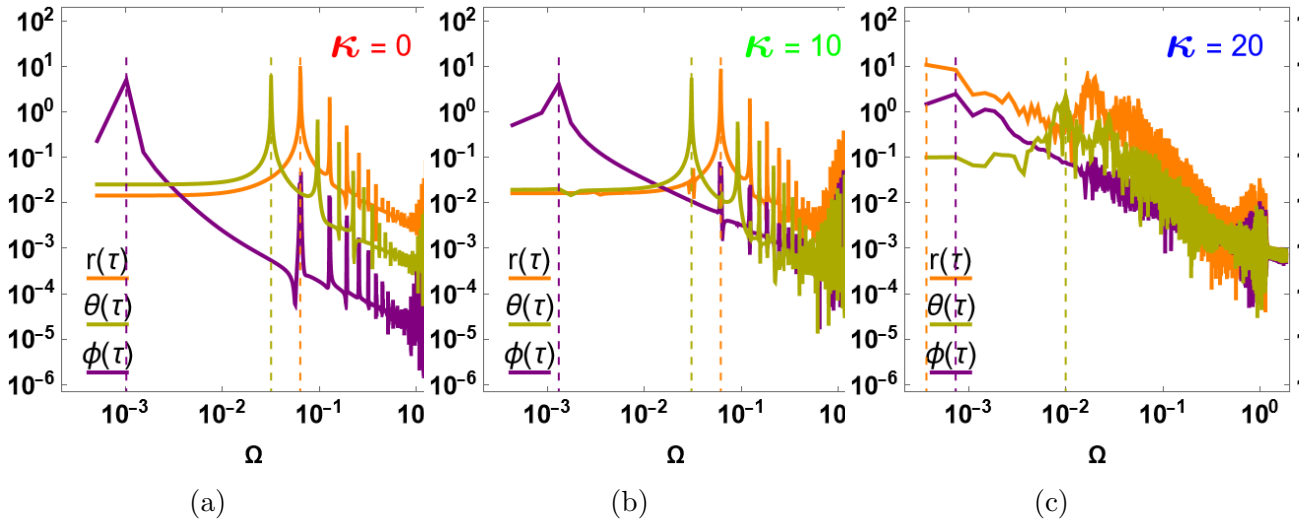


Figure 11: Power spectral density of trajectories coordinates of charged particles $r(\tau)$, $\theta(\tau)$, $\phi(\tau)$, with correspond of trajectories plotted in Fig. 10. Peaks of the fundamental frequencies of particles' motion near the circular orbits are represented as dashed lines.

Furthermore, in contrast, for the case $\kappa = 0$, the Keplerian component dominates at low frequencies, with radial and latitudinal components taking over at higher frequencies, especially the radial component. As κ increases, the frequency peaks of all trajectory coordinates tend to converge toward higher frequencies, indicating the onset of chaotic dynamics dominated by strong radial oscillations. This progression reveals how increasing κ enhances the chaotic character of particle motion. As seen in Fig. 10, this behavior is associated with particles having specific energies below 1, which remain gravitationally bound and orbit close to the BH. Their corresponding PSDs exhibit more complex, broadband features, reflecting the increased dynamical instability introduced by the CDM halo.

By studying the fundamental frequencies—radial, latitudinal, and Keplerian—we have shown how both the magnetic field and CDM environment significantly impact the stability and structure of particle motion. In particular, the CDM halo modifies the confinement regions and enhances the chaotic behavior of bound orbits, especially as the density parameter κ increases. Building on this analysis, we now turn our attention to the concept of *resonance radii*, which play a critical role in understanding QPOs. These special radii correspond to locations where characteristic frequency ratios (such as 3:2) occur, leading to resonant amplification of oscillatory modes in the accretion flow around compact objects.

4.2 Resonance Radii

HF QPOs are among the most intriguing phenomena observed in X-ray binaries (XBs), particularly in low-mass X-ray binaries (LMXBs) hosting stellar-mass BHs or neutron stars. Detected by X-ray observatories such as RXTE, NICER, and XMM-Newton, HF QPOs typically manifest as twin peaks in the Fourier power spectrum, corresponding to an upper and a lower frequency, denoted by f_U and f_L , respectively [1, 60]. In microquasars, these twin peaks often appear in a near 3:2 frequency ratio, a feature that has been interpreted as a signature of resonance phenomena occurring in the inner regions of the accretion disk [4, 49, 61].

Generally, HF QPOs are understood to be accretion disk phenomena, closely linked to the fundamental frequencies of particle motion in the strong-field regime of gravity. They provide a powerful diagnostic tool for probing spacetime geometry in the proximity compact objects. Within the framework of our study, considering a BH immersed in a uniform magnetic field and

enclosed by a CDM halo, this combination offers a rich and promising context for investigating the dynamical origin of HF QPOs. In particular, it allows us to explore how modifications to the effective potential, caused by magnetic and dark-matter interactions, can affect particle oscillations near the ISCO, where HF QPOs are believed to originate.

The presence of a CDM halo, in addition to altering the gravitational potential, can shift the ISCO radius and perturb the epicyclic frequencies of particles in the accretion disk [46, 56]. These changes could have observable consequences for the frequencies of HF QPOs and offer a potential justification for deviations from the standard 3:2 ratio in some systems. Thus, incorporating both magnetic field effects and CDM contributions enhances our understanding of the complex physics governing QPO generation in LMXBs.

The observed QPOs in XBs are associated with fundamental frequencies of particle motion in the inner accretion disk: the radial frequency ν_r , the latitudinal (vertical) frequency ν_θ , and the Keplerian (orbital) frequency ν_ϕ . Multiple theoretical models have been suggested to explain the origin of these QPOs, each characterized by different combinations of these frequencies. A detailed discussion of these models is provided below.

The model of *epicyclic resonance* (ER), originally proposed by Abramowicz and Kluzniak [4], interprets HF QPOs as a result of non-linear resonances between radial and vertical epicyclic oscillations of matter in the inner regions of the accretion disk around a compact object. In this framework, small perturbations around nearly circular and equatorial geodesics in a relativistic potential can lead to oscillations characterized by epicyclic frequencies. When these frequencies enter into a rational ratio (most notably 3:2), nonlinear resonances can be triggered. The observed twin peaks of the HF QPOs are then interpreted as arising from these resonances. Several variants of the ER model exist, depending on the identification of the upper and lower frequencies f_U and f_L with combinations of ν_r and ν_θ , as summarized in Tab. 1.

One widely studied model is the *relativistic precession* (RP) model, which attributes QPOs to relativistic corrections in particle orbits near the BH. This model does not rely on strong magnetic fields or resonance radii. Instead, it considers blobs of plasma within the accretion disk following slightly eccentric and tilted geodesics. In this framework, QPOs arise from small perturbations in the motion of these blobs, governed by the spacetime's intrinsic frequencies. In such a RP model, the upper HF QPO frequency is identified via the Keplerian frequency in the innermost regions of the disk: $f_U = \nu_\phi$. The lower HF QPO, f_L , is associated with the periastron precession of slightly eccentric orbits, defined as $f_L = \nu_\phi - \nu_r$, where ν_r is the radial epicyclic frequency. Since $\nu_r < \nu_\phi$, this difference captures the orbital precession. Additionally, horizontal branch oscillations (HBOs) are attributed to nodal precession, described by $\nu_\phi - \nu_\theta$, which reflects vertical oscillations due to frame dragging in rotating BH configurations. However, in our case the frame dragging is absent. This implies $\nu_\theta = \nu_\phi$, and thus the frequency of nodal precession vanishes. As a result, the frequency of periastron precession $f_L = \nu_\phi - \nu_r$ becomes the dominant contributor to the lower QPO of the HF over a wide range of parameters [62, 63].

Another relevant framework is the *Warped Disk* (WD) model, which addresses QPO generation in geometrically warped accretion disks. Although most accretion disk models assume equatorial symmetry, both theoretical and observational evidence support the existence of warped disks around stellar-mass and supermassive BHs [64]. The WD model involves resonant interactions between radial and vertical motions, incorporating both gravity (g-mode) and pressure (p-mode) oscillations. Horizontal resonances appear in the g- and p-modes, while vertical resonances are exclusive to the g-mode oscillations [63].

In summary, both the RP and WD models interpret QPOs as a result of oscillatory behavior within the accretion disk. Concerning our study, featuring a BH embedded in a magnetic and dark-matter environment, these frequency relations and their perturbations are crucial for identifying possible resonance conditions, especially in relation to the observed 3:2 HF QPO

frequency ratio.

Lastly, the *tidal disruption* (TD) model interprets HF QPOs as resulting from the tidal disruption of clumps of matter (blobs or inhomogeneities) in the accretion disk by the gravitational field of the BH [65, 66]. In this scenario, the orbital motion and deformation of these clumps generate periodic modulations in the X-ray flux. Concerning f_U and f_L of such a model, the observed modulation is produced by a combination of v_ϕ and v_r , which reflects the rate of deformation or compression due to the tidal force. This model has the advantage of offering a more physically intuitive mechanism: actual matter structures are being distorted by gravity and magnetic effects, causing quasi-periodic emission patterns. The model is particularly useful in systems where strong radial motion is expected, such as near the innermost regions of thick accretion disks or in the presence of non-axisymmetric perturbations.

Model	Label	Upper Frequency $f_U(r)$	Lower Frequency $f_L(r)$
<i>Epicyclic Resonance</i> (ER)	ER0	v_θ	v_r
	ER1	v_θ	$v_\theta - v_r$
	ER2	$v_\theta - v_r$	v_r
	ER3	$v_\theta + v_r$	v_θ
	ER4	$v_\theta + v_r$	$v_\theta - v_r$
	ER5	v_r	$v_\theta - v_r$
<i>Relativistic Precession</i> (RP)	RP0	v_ϕ	$v_\phi - v_r$
	RP1	v_θ	$v_\phi - v_r$
	RP2	v_ϕ	$v_\theta - v_r$
<i>Tidal Disruption</i> (TD)	TD	$v_\phi + v_r$	v_ϕ
<i>Warped Disk</i> (WD)	WD	$2v_\phi - v_r$	$2(v_\phi - v_r)$

Table 1: *Frequency identification schemes for various QPO models. Each model defines the upper and lower observed frequencies $f_U(r)$ and $f_L(r)$ in terms of fundamental frequencies of particle motion.*

The twin peaks of $f_U:f_L$ of HF QPOs are in function of the BH mass M , B' strength, and the parameter that controls the DM halo κ . Fig 12 represents the radial profiles of $f_U(r)$ and $f_L(r)$ for various HF QPOs models such as epical resonance ER, RP, TD, and WD.

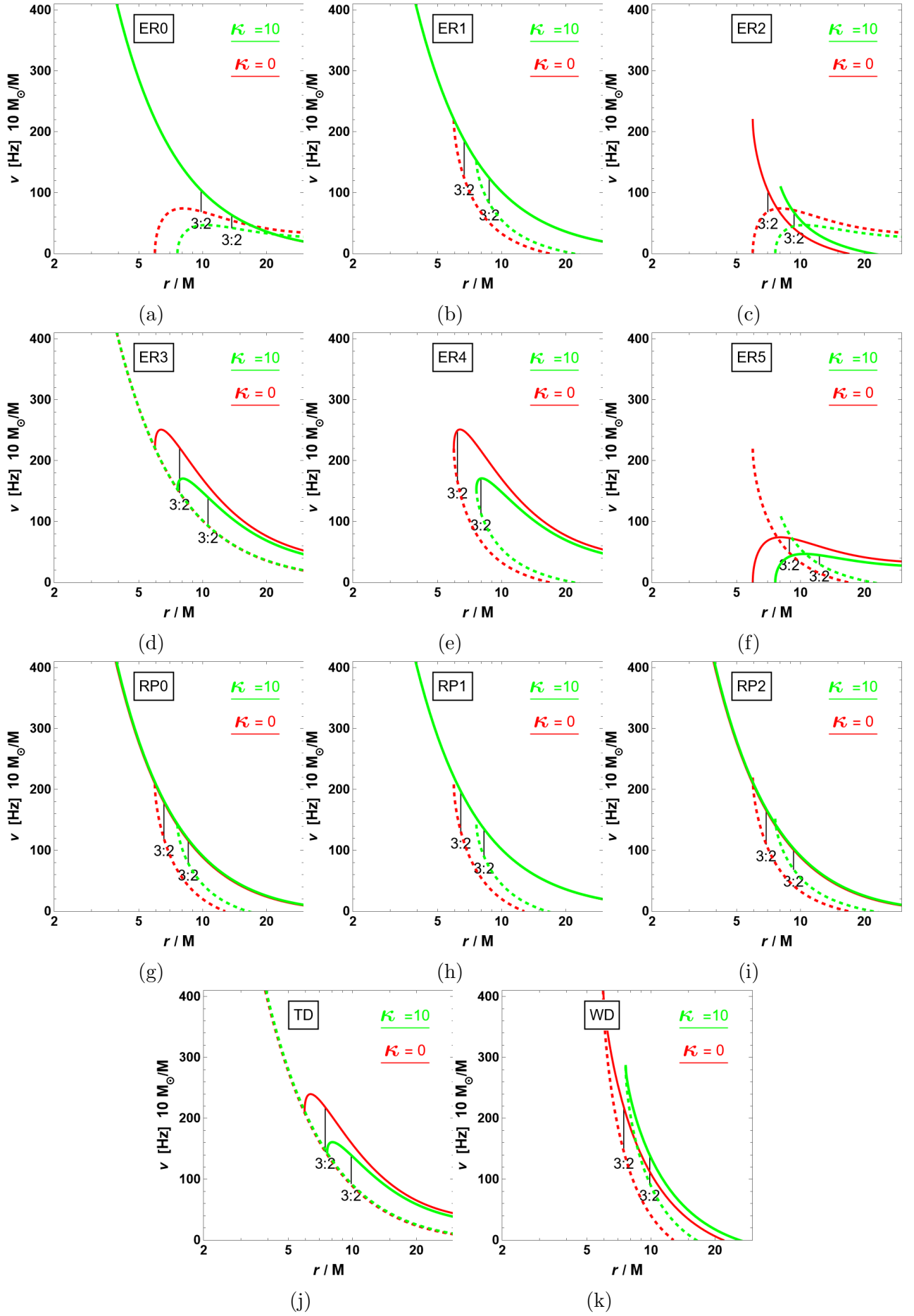


Figure 12: Radial profiles of lower $\nu_L(r)$ and upper $\nu_U(r)$ frequencies for several HF QPOs models, with different values of density profile κ within $R_s = 1000$ on weak magnetic field of strength $B' = 0.01$ in all cases, The Displacement $f_U(r) : f_L(r) = 3:2$ of resonance radii also plotted

From Fig.12, one can notice that the locations of the 3:2 resonance radii vary significantly across different models. Among them, the ER0 model exhibits the largest resonance radius, located at $r = 9.83589$ for $\kappa = 0$, and shifting outward to $r = 13.7114$ for $\kappa = 10$. In contrast, the ER4 model yields the smallest resonance radius, with $r = 6.19465$ for $\kappa = 0$, and $r = 7.98434$ when $\kappa = 10$. For more details, we provide Table 2, which lists the positions of the resonance radii for the different models, evaluated at various values of CDM density.

Model	$\kappa = 0$	$\kappa = 5$	$\kappa = 10$	$\kappa = 15$	$\kappa = 20$
ER0	9.835 89	11.6557	13.7114	15.9826	18.4565
ER1	6.661 94	7.6306	8.740 95	10.0102	11.4554
ER2	7.0205	8.091 17	9.327 46	10.7485	12.3714
ER3	7.784 82	9.083 74	10.6015	12.3589	14.3709
ER4	6.194 65	7.034 26	7.984 34	9.057 39	10.2665
ER5	8.864 29	10.4525	12.2827	14.3491	16.6405
RP0	6.570 77	7.497 89	8.549 67	9.737 96	11.0739
RP1	6.420 45	7.286 62	8.256 78	9.338 31	10.5381
RP2	6.890 08	7.980 11	9.276 71	10.8297	12.7011
TD	7.448 65	8.581 49	9.866 33	11.3099	12.9161
WD	7.448 65	8.581 49	9.866 33	11.3099	12.9161

Table 2: *Resonance Radius Variation Across Different Models, Each model defines the location of the resonance radius for both cases: without DM ($\kappa = 0$) and with DM ($\kappa = 5, 10, 15, 20$).*

These results demonstrate that the presence of CDM leads to a systematic outward shift of the resonance radii, reflecting the influence of the halo’s density on the gravitational potential near the BH.

Next, to explore some astrophysical implications, it’s essential to assess whether the models examined can reproduce the HF QPOs observed in real astrophysical systems.

5 On some astrophysical estimations of HF QPOs

In this section, we perform a comparative examination between theoretical model predictions and observational data from well-known microquasars, serving as a testbed to assess the viability of our framework in the presence of a CDM halo.

One of the notable effects attributed to CDM is the enhancement of a BH’s gravitational potential, which may contribute to explaining HF QPOs observed in accreting systems [44, 49]. To investigate this, we fit the HF QPO data of four microquasars—GRS 1915+105, H1743-322, XTE 1550-564, and GRO 1655-40—summarized in Table 3, under the assumption of non-rotating BHs [36]. Our analysis focuses on four representative models: the ER, RP, TD, and

	GRS 1915+105	H1743-322	XTE 1550-564	GRO 1655-40
$M [M_{\odot}]$	9.6 – 18.4	9.25 – 12.86	8.5 – 9.7	6.03 – 6.57
ν_U [Hz]	165 – 171	237 – 243	273 – 279	447 – 453
ν_L [Hz]	108 – 118	158 – 174	179 – 189	295 – 305

Table 3: *Observed twin HF QPOs data for the four microquasars, the mass, upper and lower frequencies [67–69].*

the WD models.

In Fig.13, we perform a fitting of the observed HF QPO f_U through distinct theoretical models, evaluated at the 3:2 resonance radii for distinct values of the CDM density parameter κ . The analysis is carried out across multiple intensity of B , allowing us to assess the influence of both CDM and magnetic fields on the predicted QPO frequencies.

Fig.13 unveils that the TD and WD models appear to be more realistic, fitting the majority of the observational data better than other models such as ER and RP in the case of a uniform magnetic field with strength $B' = 0.1$. Where the GRS 1915-105 fit all the cases of CDM density, whereas H1743-322 fit three cases of CDM corresponding to $\kappa = 0, 5, 10$, the last microquasar doesn't fit any of proposed cases. In contrast, for vanishing and weaker magnetic fields ($B' = 0$ and $B' = 0.01$), all models, except ER, provide a good description of the microquasar GRS 1915+105, TD and WD fit the GRS 1915-105 in the absence of CDM and the presence of weak density approximation (e.g $\kappa = 5$). For RP model, only fit it where $\kappa = 0$. Notably, the ER model fails to fit any observational data from Table 3 under low magnetic field conditions. It is also worth mentioning that the TD and WD models yield identical results.

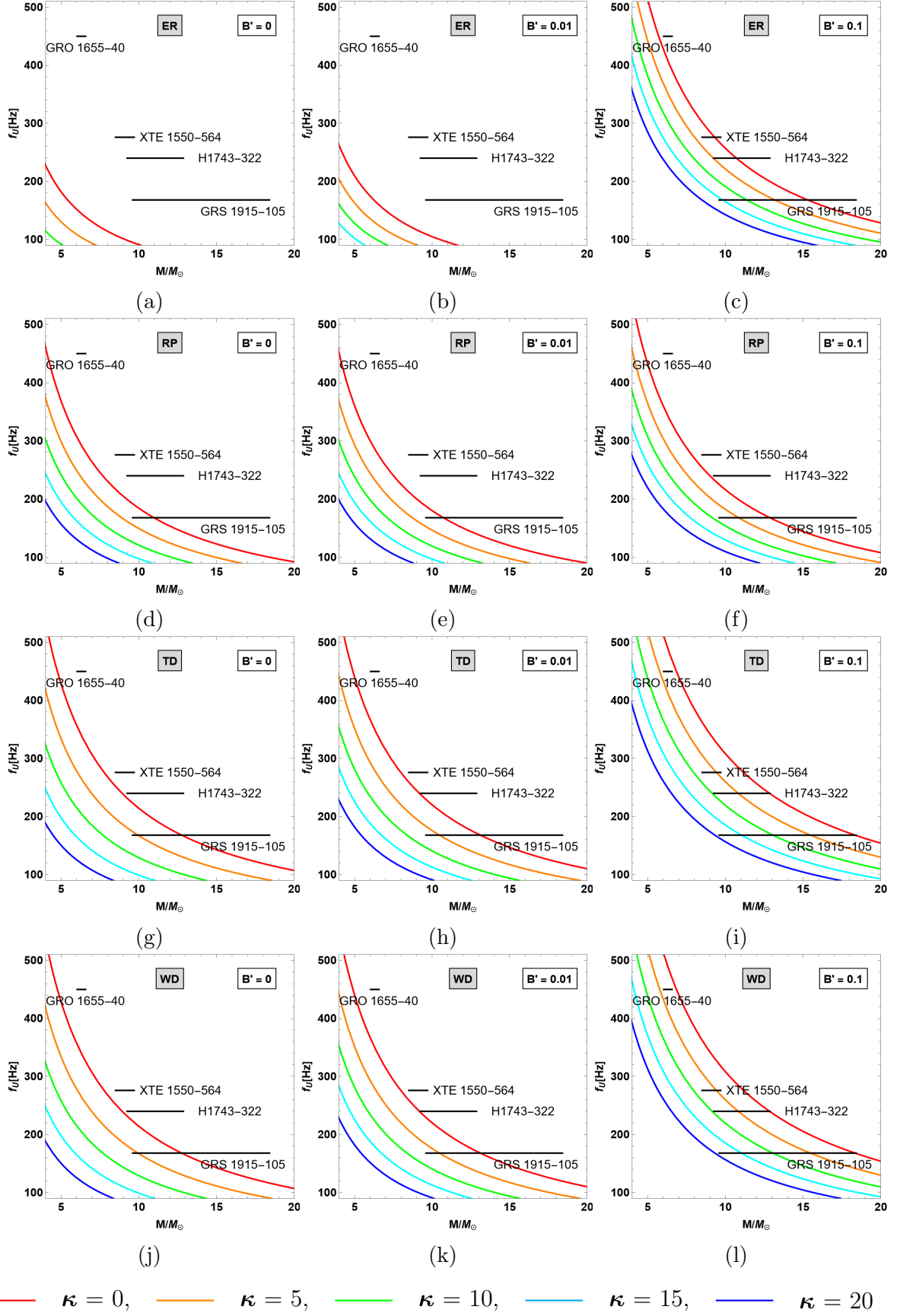


Figure 13: Fitting the observed HF QPOs frequencies in different models of the upper oscillation frequency f_U at the resonance radii 3 : 2 for different values of κ within $R_s = 1000$ for different cases of magnetic field strength B

6 Conclusion and Discussion

Charged particle trajectories close to a BH can generally be classified into three cases: particles can spiral into the BH, tends to infinite space, or orbit stably in circular trajectories around the BH. However, the behavior of these motions differs depending on whether the particles are charged or neutral, as well as on the nature of the spacetime in the region of the BH.

Throughout this study, we consider a Schwarzschild BH embedded in a uniform magnetic field and bordered by a CDM halo. Through our analysis of charged particle dynamics, we identified several arising from both the magnetic field and the CDM. Notably, CDM influences the BH geometry by affecting the site of the event horizon. As the CDM density increases—reflected by higher values of the parameter κ —the event horizon grows. Consequently, the effective mass of the BH increases, resulting in a stronger gravitational pull that drives charged particles inward, effectively reducing the attribution of the magnetic field in that scheme.

Moreover, the location of the ISCO varies depending on the B' strength and CDM density- κ . These two factors act in opposition; a stronger magnetic field transitions the ISCO closer to the BH, while increasing CDM density pushes the ISCO outward. This opposing influence is also observed in the stability region: B' tends to shrink the area of stability, whereas CDM expands it. In both positive and negative magnetic field cases, CDM contributes to enlarging the stability zone of charged particle motion. Indeed, at high CDM densities, the effective potential, represented by one or two boundaries depending on the sign of B' , tends to merge these boundaries. This causes to the trapping of particles near the BH, increasing their likelihood of being captured.

It's also observed that in the case of a positive uniform magnetic field, particles follow curled trajectories around the BH. The degree of this curvature increases trough the magnitude of the magnetic field. However, CDM tends to reduce the curling of these trajectories. At high intensity of B' and off the equatorial plane, ionized particle ejection (jet phenomena) can occur. CDM affects this behavior as well: as κ increases, particles are more strongly trapped near the BH. To overcome this trapping and enable particle escape, a stronger magnetic field is required for relativistic jets.

Furthermore, we have examined the harmonic oscillations of charged particles orbiting a magnetized BH surrounded by a CDM halo. Our analysis has shown that the influence of CDM is significant both at small radii, nearby to the BH, and at large distances. In particular, at large distances, the radial frequency is not affected by the magnetic field, whether it is positive or negative, when CDM surrounds the BH. Regarding resonant phenomena, we have studied the variation in the location of the resonance radii corresponding to the 3:2 ratio between higher and lower frequencies across several HF QPO models. We have found that the presence of the CDM halo shifts the resonance radii farther from the BH in all considered models, namely ER, the RP model, the TD, and the WD models.

At the end, we have performed a fitting of the QPO data observed from four microquasars—GRS 1915+105, H1743-322, XTE J1550-564, and GRO J1655-40—for different values of CDM density parameter κ and various magnetic field strengths, using numerous models: ER(ER0), RP(RP0), TD and WD. The TD and WD model provides a well suited to nearly all data at a intensity of the magnetic field of $B' = 0.1$, outperforming the RP model in this context. These results suggest that the ER, TD, and WD models be crucial to clarifying the HF QPOs observed in compact objects.

These findings motivate a deeper investigation into astrophysical processes involving Kerr and accelerating BHs, which are widely considered to be realistic models of rotating and binary BHs in the universe. A compelling open question arises: to what extent does DM contribute to the luminosity and structure of accretion disks around rotating BHs, in conjunction with the

well-established influence of magnetic fields and their varying intensities?

Acknowledgements

H. El M would like to acknowledge networking support of the COST Action CA 22113 - Fundamental challenges in theoretical physics (Theory and Challenges), CA 21136 - Addressing observational tensions in cosmology with systematics and fundamental physics (CosmoVerse), and CA 23130 - Bridging high and low energies in search of quantum gravity (BridgeQG). He also thanks IOP for its support.

References

- [1] Ronald A. Remillard and Jeffrey E. McClintock. X-ray Properties of Black-Hole Binaries. Ann. Rev. Astron. Astrophys., 44:49–92, 2006.
- [2] Tomaso M. Belloni, Andrea Sanna, and Mariano Mendez. High-Frequency Quasi-Periodic Oscillations in black-hole binaries. Mon. Not. Roy. Astron. Soc., 426:1701, 2012.
- [3] Feng Yuan and Ramesh Narayan. Hot Accretion Flows Around Black Holes. Ann. Rev. Astron. Astrophys., 52:529–588, 2014.
- [4] Marek Artur Abramowicz and Wlodek Kluzniak. A Precise determination of angular momentum in the black hole candidate GRO J1655-40. Astron. Astrophys., 374:L19, 2001.
- [5] Marek A. Abramowicz, Wlodek Kluzniak, Jeffrey E. McClintock, and Ronald A. Remillard. The Importance of discovering a 3:2 twin - peak QPO in a ULX or how to solve the puzzle of intermediate mass black holes. Astrophys. J. Lett., 609:L63–L65, 2004.
- [6] S. E. Motta, T. M. Belloni, L. Stella, T. Muñoz Darias, and R. Fender. Precise mass and spin measurements for a stellar-mass black hole through X-ray timing: the case of GRO J1655–40. Mon. Not. Roy. Astron. Soc., 437(3):2554–2565, 2014.
- [7] Luigi Stella, Mario Vietri, and Sharon Morsink. Correlations in the qpo frequencies of low mass x-ray binaries and the relativistic precession model. Astrophys. J. Lett., 524:L63–L66, 1999.
- [8] Marek A. Abramowicz, Wlodek Kluzniak, Zdenek Stuchlik, and Gabriel Torok. The Orbital resonance model for twin peak kHz QPOs: Measuring the black hole spins in microquasars. 1 2004.
- [9] Zdeněk Stuchlík and Martin Kološ. String loops oscillating in the field of Kerr black holes as a possible explanation of twin high-frequency quasiperiodic oscillations observed in microquasars. Phys. Rev. D, 89(6):065007, 2014.
- [10] Mariia Churilova, Martin Kološ, and Zdeněk Stuchlík. String loop vibration around Schwarzschild black hole. Eur. Phys. J. C, 84(1):25, 2024.
- [11] Cosimo Bambi. Testing black hole candidates with electromagnetic radiation. Rev. Mod. Phys., 89(2):025001, 2017.

- [12] G. Mustafa, Phongpichit Channuie, Faisal Javed, Abdelmalek Bouzenada, S. K. Maurya, Arzu Cilli, and Ertan Güdekli. Orbital motion and epicyclic oscillations around a black hole with magnetic charge. Phys. Dark Univ., 47:101765, 2025.
- [13] Jeffrey E. McClintock, Rebecca Shafee, Ramesh Narayan, Ronald A. Remillard, Shane W. Davis, and Li-Xin Li. The Spin of the Near-Extreme Kerr Black Hole GRS 1915+105. Astrophys. J., 652:518–539, 2006.
- [14] Tim Johannsen and Dimitrios Psaltis. Testing the No-Hair Theorem with Observations in the Electromagnetic Spectrum: II. Black-Hole Images. Astrophys. J., 718:446–454, 2010.
- [15] P. A. R. Ade et al. Planck 2015 results. XIII. Cosmological parameters. Astron. Astrophys., 594:A13, 2016.
- [16] James S. Bullock and Michael Boylan-Kolchin. Small-Scale Challenges to the Λ CDM Paradigm. Ann. Rev. Astron. Astrophys., 55:343–387, 2017.
- [17] Sacha Davidson and Michael E. Peskin. Astrophysical bounds on millicharged particles in models with a paraphoton. Phys. Rev. D, 49:2114–2117, 1994.
- [18] Pawan Kumar Gupta, Thomas F. M. Spieksma, Peter T. H. Pang, Gideon Koekoek, and Chris Van Den Broeck. Bounding dark charges on binary black holes using gravitational waves. Phys. Rev. D, 104(6):063041, 2021.
- [19] Wan-Zhe Feng, Zi-Hui Zhang, and Kai-Yu Zhang. Sub-GeV millicharge dark matter from the $U(1)_X$ hidden sector. JCAP, 05:112, 2024.
- [20] Audrey Fung, Saniya Heeba, Qinrui Liu, Varun Muralidharan, Katelin Schutz, and Aaron C. Vincent. New bounds on light millicharged particles from the tip of the red-giant branch. Phys. Rev. D, 109(8):083011, 2024.
- [21] Asher Berlin, Raffaele Tito D’Agnolo, Sebastian A. R. Ellis, and Jury I. Radkovski. Signals of millicharged dark matter in light-shining-through-wall experiments. JHEP, 08:017, 2023.
- [22] Gianfranco Bertone, Dan Hooper, and Joseph Silk. Particle dark matter: Evidence, candidates and constraints. Phys. Rept., 405:279–390, 2005.
- [23] Stacy Y. Kim, Annika H. G. Peter, and Jonathan R. Hargis. Missing Satellites Problem: Completeness Corrections to the Number of Satellite Galaxies in the Milky Way are Consistent with Cold Dark Matter Predictions. Phys. Rev. Lett., 121(21):211302, 2018.
- [24] Michael Boylan-Kolchin, James S. Bullock, and Manoj Kaplinghat. Too big to fail? The puzzling darkness of massive Milky Way subhaloes. Mon. Not. Roy. Astron. Soc., 415:L40, 2011.
- [25] Bing-Qiang Qiao, Qing Luo, Qiang Yuan, and Yi-Qing Guo. Understanding the Phase Reversals of Galactic Cosmic-Ray Anisotropies. Astrophys. J., 942(1):13, 2023.
- [26] Yiran Zhang and Siming Liu. Small-scale Anisotropies of Cosmic Rays from Turbulent Flow. Astrophys. J. Lett., 964(1):L1, 2024.
- [27] Kazunori Akiyama et al. First M87 Event Horizon Telescope Results. I. The Shadow of the Supermassive Black Hole. Astrophys. J. Lett., 875:L1, 2019.

- [28] Kazunori Akiyama et al. First Sagittarius A* Event Horizon Telescope Results. I. The Shadow of the Supermassive Black Hole in the Center of the Milky Way. Astrophys. J. Lett., 930(2):L12, 2022.
- [29] Martin J. Rees. Black Hole Models for Active Galactic Nuclei. Ann. Rev. Astron. Astrophys., 22:471–506, 1984.
- [30] D. Richstone et al. Supermassive black holes and the evolution of galaxies. Nature, 395:A14–A19, 1998.
- [31] Laleh Sadeghian, Francesc Ferrer, and Clifford M. Will. Dark matter distributions around massive black holes: A general relativistic analysis. Phys. Rev. D, 88(6):063522, 2013.
- [32] Enrico Barausse, Vitor Cardoso, and Paolo Pani. Can environmental effects spoil precision gravitational-wave astrophysics? Phys. Rev. D, 89(10):104059, 2014.
- [33] D. Pugliese, H. Quevedo, and R. Ruffini. Circular motion of neutral test particles in Reissner-Nordström spacetime. Phys. Rev. D, 83:024021, 2011.
- [34] Chen-Yu Liu, Da-Shin Lee, and Chi-Yong Lin. Geodesic motion of neutral particles around a Kerr–Newman black hole. Class. Quant. Grav., 34(23):235008, 2017.
- [35] Ming Zhang and Wen-Biao Liu. Innermost stable circular orbits of charged spinning test particles. Phys. Lett. B, 789:393–398, 2019.
- [36] Martin Kološ, Zdeněk Stuchlík, and Arman Tursunov. Quasi-harmonic oscillatory motion of charged particles around a schwarzschild black hole immersed in a uniform magnetic field. Classical and Quantum Gravity, 32(16):165009, 2015.
- [37] Martin Kološ, Misbah Shahzadi, and Arman Tursunov. Charged particle dynamics in parabolic magnetosphere around schwarzschild black hole. The European Physical Journal C, 83(4):323, 2023.
- [38] Zdeněk Stuchlík and Martin Kološ. Acceleration of the charged particles due to chaotic scattering in the combined black hole gravitational field and asymptotically uniform magnetic field. The European Physical Journal C, 76:1–21, 2016.
- [39] Xin Sun, Xin Wu, Yu Wang, Chen Deng, Baorong Liu, and Enwei Liang. Dynamics of charged particles moving around kerr black hole with inductive charge and external magnetic field. Universe, 7(11):410, 2021.
- [40] M. Yu. Piotrovich, N. A. Silant’ev, Yu. N. Gnedin, and T. M. Natsvlishvili. Magnetic fields of black holes and the variability plane, 2010.
- [41] Robert M Wald. Black hole in a uniform magnetic field. Physical Review D, 10(6):1680, 1974.
- [42] Prerna Rana and A Mangalam. Astrophysically relevant bound trajectories around a kerr black hole. Classical and Quantum Gravity, 36(4):045009, 2019.
- [43] Zdeněk Stuchlík, Martin Kološ, and Arman Tursunov. Magnetized black holes: ionized keplerian disks and acceleration of ultra-high energy particles. Multidisciplinary Digital Publishing Institute Proceedings, 17(1):13, 2019.

- [44] Misbah Shahzadi, Martin Kološ, Zdeněk Stuchlík, and Yousaf Habib. Epicyclic oscillations in spinning particle motion around kerr black hole applied in models fitting the quasi-periodic oscillations observed in microquasars and agns. The European Physical Journal C, 81(12):1067, 2021.
- [45] Sanjar Shaymatov, Daniele Malafarina, and Bobomurat Ahmedov. Effect of perfect fluid dark matter on particle motion around a static black hole immersed in an external magnetic field. Physics of the Dark Universe, 34:100891, 2021.
- [46] Bakhtiyor Narzilloev, Javlon Rayimbaev, Sanjar Shaymatov, Ahmadjon Abdujabbarov, Bobomurat Ahmedov, and Cosimo Bambi. Dynamics of test particles around a bardeen black hole surrounded by perfect fluid dark matter. Physical Review D, 102(10):104062, 2020.
- [47] Asifa Ashraf, Tayyab Naseer, Himanshu Chaudhary, Abdelmalek Bouzenada, Farruh Atamurotov, Batuhan Çil, and Ertan Güdekli. Observational constraints on qpos with orbital motion around charged non-commutative schwarzschild black hole surrounded by perfect fluid dark matter. Nuclear Physics B, page 116873, 2025.
- [48] Kuantay Boshkayev, Anuar Idrissov, Orlando Luongo, and Daniele Malafarina. Accretion disc luminosity for black holes surrounded by dark matter. Monthly Notices of the Royal Astronomical Society, 496(2):1115–1123, 2020.
- [49] Gabriel Török, Marek A Abramowicz, W Kluźniak, and Z Stuchlík. The orbital resonance model for twin peak khz quasi periodic oscillations in microquasars. Astronomy & Astrophysics, 436(1):1–8, 2005.
- [50] Jaroslav Vrba, Javlon Rayimbaev, Zdenek Stuchlik, and Bobomurat Ahmedov. Charged particles motion and quasiperiodic oscillation in simpson–visser spacetime in the presence of external magnetic fields. The European Physical Journal C, 83(9):854, 2023.
- [51] Tursunali Xamidov, Sanjar Shaymatov, Bobomurat Ahmedov, and Tao Zhu. Probing quantum corrected black hole through astrophysical tests with the orbit of s2 star and quasiperiodic oscillations. arXiv preprint arXiv:2503.06750, 2025.
- [52] John Dubinski and RG Carlberg. The structure of cold dark matter halos. Astrophysical Journal, Part 1 (ISSN 0004-637X), vol. 378, Sept. 10, 1991, p. 496-503. Research supported by Pittsburgh Supercomputing Center and NSERC., 378:496–503, 1991.
- [53] Julio F Navarro. The structure of cold dark matter halos. In Symposium-international astronomical union, volume 171, pages 255–258. Cambridge University Press, 1996.
- [54] Julio F. Navarro, Carlos S. Frenk, and Simon D. M. White. The Structure of cold dark matter halos. Astrophys. J., 462:563–575, 1996.
- [55] Julio F. Navarro, Carlos S. Frenk, and Simon D. M. White. A Universal density profile from hierarchical clustering. Astrophys. J., 490:493–508, 1997.
- [56] Zhaoyi Xu, Xian Hou, Xiaobo Gong, and Jiancheng Wang. Black hole space-time in dark matter halo. Journal of Cosmology and Astroparticle Physics, 2018(09):038–038, September 2018.
- [57] Valeri P Frolov and Andrey A Shoom. Motion of charged particles near a weakly magnetized schwarzschild black hole. Physical Review D—Particles, Fields, Gravitation, and Cosmology, 82(8):084034, 2010.

- [58] Mai Qi, Javlon Rayimbaev, and Bobomurat Ahmedov. Charged particles and quasiperiodic oscillations around magnetized schwarzschild black holes. The European Physical Journal C, 83(8):730, 2023.
- [59] Valeri P. Frolov and Andrey A. Shoom. Motion of charged particles near weakly magnetized Schwarzschild black hole. Phys. Rev. D, 82:084034, 2010.
- [60] M. van der Klis. Rapid X-ray variability, pages 39–112. Cambridge Astrophysics. Cambridge University Press, Cambridge, 2006.
- [61] S. E. Motta, T. Muñoz Darias, A. Sanna, R. Fender, T. Belloni, and L. Stella. Black hole spin measurements through the relativistic precession model: XTE J1550-564. Mon. Not. Roy. Astron. Soc., 439:65, 2014.
- [62] Luigi Stella, Mario Vietri, and Sharon M Morsink. Correlations in the quasi-periodic oscillation frequencies of low-mass x-ray binaries and the relativistic precession model. The Astrophysical Journal, 524(1):L63, 1999.
- [63] Bidyut Hazarika, Mrinmoy M Gohain, and Prabwal Phukon. Signatures of ned on quasi periodic oscillations of a magnetically charged black hole. arXiv preprint arXiv:2504.07821, 2025.
- [64] Scott Tremaine and Shane W Davis. Dynamics of warped accretion discs. Monthly Notices of the Royal Astronomical Society, 441(2):1408–1434, 2014.
- [65] C. Germana, U. Kostic, A. Cadez, and M. Calvani. Tidal disruption of small satellites orbiting black holes. AIP Conf. Proc., 1126(1):367–369, 2009.
- [66] U. Kostic, A. Cadez, M. Calvani, and A. Gomboc. Tidal effects on small bodies by massive black holes. Astron. Astrophys., 496:307, 2009.
- [67] Ronald A Remillard and Jeffrey E McClintock. X-ray properties of black-hole binaries. Annu. Rev. Astron. Astrophys., 44(1):49–92, 2006.
- [68] Aslam Ali Molla, Sandip K Chakrabarti, Dipak Debnath, and Santanu Mondal. Estimation of mass of compact object in h 1743-322 from 2010 and 2011 outbursts using tcdf solution and spectral index–qpo frequency correlation. The Astrophysical Journal, 834(1):88, 2017.
- [69] Adam Ingram and Sara Motta. Solutions to the relativistic precession model. Monthly Notices of the Royal Astronomical Society, 444(3):2065–2070, 2014.